

THESIS FOR THE DEGREE OF DOCTOR OF PHILOSOPHY

**THIN FILMS AND COMPONENT  
TECHNOLOGIES FOR LOW-NOISE  
TERAHERTZ ELECTRONICS**

Dimitar M. Dochev



Group for Advanced Receiver Development  
Department of Earth and Space Sciences  
Chalmers University of Technology  
Göteborg, Sweden 2010

Thin Films and Component Technologies  
for Low-Noise Terahertz Electronics  
DIMITAR M. DOCHEV  
ISBN 978-91-7385-473-3

© DIMITAR M. DOCHEV, 2010

Doktorsavhandlingar vid Chalmers tekniska högskola  
Ny serie nr 3154  
ISSN 0346-718X

Group for Advanced Receiver Development  
Department of Earth and Space Sciences  
Chalmers University of Technology  
SE-412 96 Göteborg  
Sweden  
Telephone + 46 (0)31-772 1000

Cover: An SEM composite image of a balanced waveguide HEB mixer for 1.6-2.0 THz. Top right: close-up of the mixer chip across the waveguide. Bottom left: close-up of a waveguide branch-line coupler.

Printed by Chalmers Reproservice  
Göteborg, Sweden 2010

**Thin Films and Component Technologies  
for Low-Noise Terahertz Electronics**  
DIMITAR M. DOCHEV  
Department of Earth and Space Sciences  
Chalmers University of Technology

## **Abstract**

This thesis deals with several distinct subjects such as thin film deposition, design, fabrication and characterization of components for low-noise THz electronics.

High energy-gap superconducting materials are of specific importance for low-noise THz mixer applications. Extending the upper operation frequency of superconductor-insulator-superconductor (SIS) mixers above 1.5 THz is of particular interest. Here, a novel approach of producing Nb<sub>3</sub>Al thin film based on DC magnetron co-sputtering using heteroepitaxial, as well as epitaxial growth techniques, has been employed. As a result, a superconducting transition temperature, as high as 15.7 K has been observed. Structural and electrical characterization techniques have been utilized to evaluate the set of material and superconducting parameters of the deposited Nb<sub>3</sub>Al thin films. The superconducting properties of the obtained Nb<sub>3</sub>Al films have revealed strong potential for using them in practical applications. It has been also demonstrated that Nb<sub>3</sub>Al can be epitaxially grown on yttria-stabilized-zirconia substrates, thus opening a possibility for hot-electron bolometer (HEB) applications.

Another substantial part of this work deals with the in-house development of phonon-cooled HEB mixers. A reliable deposition process for high-quality ultra-thin NbN films has been established. Epitaxial ultra-thin NbN films grown on 3C-SiC/Si substrate with state-of-the-art performance have shown a strong potential to be used in THz HEB mixers with a purpose for improving the intermediate frequency (IF) bandwidth. A novel membrane-like layout for 1.6-2.0 THz HEB mixer has been suggested, developed and implemented for use with micromachined all-metal waveguides.

Being the most used in mm- and submillimeter mixer technology for radio astronomy, Nb/Al-AIO<sub>x</sub>/Nb tunnel junction stability properties are of great importance. In this thesis, the behaviour of a large number high-quality Nb/Al-AIO<sub>x</sub>/Nb tunnel junctions, subjected to long-term room temperature aging and thermal annealing is systematically studied and explanations of the observed phenomena are suggested.

Finally, the work on development of a planar superconducting IF/biasing circuit for use with a SIS mixer is presented. The circuit was integrated into a 385-500 GHz DSB SIS mixer currently under operation at the APEX telescope. Circuit design methodology, measurement results and overall mixer performance with the integrated circuit are shown.

**Keywords:** epitaxial film, hot electron bolometer, microwave circuits, Nb<sub>3</sub>Al, NbN, SIS, superconductor, THz electronics, thin film, tunnel junctions.



# List of Appended Papers

This thesis is based on the following papers:

- A. Nb<sub>3</sub>Al thin film deposition for low-noise terahertz electronics**  
D. Dochev, A. B. Pavolotsky, V. Belitsky, and H. Olofsson  
*Journal of Physics: Conference Series* **97**, 012072 (2008)
- B. The effect of aging and annealing on the properties of Nb/Al-AIO<sub>x</sub>/Nb tunnel junctions**  
D. Dochev, A. B. Pavolotsky, Z. Lai, and V. Belitsky  
*Journal of Physics: Conference Series* **234**, 042006 (2010)
- C. Aging- and annealing-induced variations of Nb/Al-AIO<sub>x</sub>/Nb tunnel junction properties**  
A. B. Pavolotsky, D. Dochev, and V. Belitsky  
*Submitted to Journal of Applied Physics* (2010)
- D. Superconducting IF biasing circuit for low-noise cryogenic applications**  
D. Dochev, R. Monje, V. Vassilev, and V. Belitsky  
*Journal of Physics: Conference Series* **234**, 042007 (2010)
- E. Growth and characterization of epitaxial ultra-thin NbN films on 3C-SiC/Si substrate for terahertz applications**  
D. Dochev, V. Desmaris, A. B. Pavolotsky, D. Meledin, Z. Lai, A. Henry, E. Janzén, E. Pippel, J. Woltersdorf, and V. Belitsky  
*Submitted to Superconductor Science and Technology* (2010)
- F. A technology demonstrator for 1.6-2.0 THz waveguide HEB receiver with a novel mixer layout**  
D. Dochev, V. Desmaris, D. Meledin, A. B. Pavolotsky, and V. Belitsky  
*Manuscript* (2010)

## Other Papers

The following papers are not included due to an overlap in contents or a content which goes beyond the scope of this thesis:

- 1. A 1.3 THz balanced waveguide HEB mixer for the APEX telescope**  
D. Meledin, A. Pavolotsky, V. Desmaris, I. Lapkin, C. Risacher, V. Perez, D. Henke, O. Nyström, E. Sundin, D. Dochev, M. Pantaleev, M. Strandberg, B. Voronov, G. Gol'tsman, and V. Belitsky  
*IEEE Transactions on Microwave Theory and Techniques* **57**, 89 (2009)
- 2. Optics design and verification for the APEX Swedish Heterodyne Facility Instrument (SHeFI)**  
O. Nyström, I. Lapkin, V. Desmaris, D. Dochev, S-E. Ferm, M. Fredrixon, D. Henke, D. Meledin, R. Monje, M. Strandberg, E. Sundin, V. Vassilev, and V. Belitsky  
*International Journal of Infrared, Millimeter and Terahertz Waves* **30**, 746 (2009)
- 3. Optics design and verification for the APEX Swedish Heterodyne Facility Instrument (SHeFI)**  
I. Lapkin, O. Nyström, V. Desmaris, D. Meledin, D. Dochev, V. Vassilev, M. Strandberg, R. Monje, D. Henke, E. Sundin, S-E. Ferm, M. Fredrixon, and V. Belitsky  
*Proc. 19<sup>th</sup> Int. Symp. Space THz Tech.* **1**, 351 (2008)
- 4. A 0.5 THz sideband separation SIS mixer for APEX telescope**  
R. Monje, V. Belitsky, V. Vassilev, A. Pavolotsky, I. Lapkin, V. Desmaris, D. Meledin, D. Henke, and D. Dochev  
*Proc. 19<sup>th</sup> Int. Symp. Space THz Techn.* **2**, 439 (2008)
- 5. Low-noise cryogenic amplifier built using hybrid MMIC-like/TRL technique**  
O. Nyström, E. Sundin, D. Dochev, V. Desmaris, V. Vassilev, and V. Belitsky  
*GigaHertz Symposium*, Göteborg, Sweden (2008).
- 6. A Swedish heterodyne facility instrument for the APEX telescope**  
V. Vassilev, D. Meledin, I. Lapkin, V. Belitsky, O. Nyström, D. Henke, A. Pavolotsky, R. Monje, C. Risacher, M. Olberg, M. Strandberg, E. Sundin, M. Fredrixon, S-E. Ferm, V. Desmaris, D. Dochev, M. Pantaleev, P. Bergman, and H. Olofsson  
*Astronomy and Astrophysics* **490**, 1157 (2008)

**7. Facility Heterodyne Receiver for the Atacama Pathfinder Experiment Telescope**

V. Belitsky, I. Lapkin, V. Vassilev, R. Monje, A. Pavolotsky, D. Meledin, D. Henke, O. Nyström, V. Desmaris, C. Risacher, M. Svensson, M. Olberg, E. Sundin, M. Fredrixon, D. Dochev, S-E. Ferm, and H. Olofsson

*Proc. Joint 32<sup>nd</sup> Int. Conf. Infrared Millimeter Waves and 15<sup>th</sup> Int. Conf. Terahertz Electronics* (2007)

**8. A 211–275 GHz sideband separating SIS mixer for APEX**

V. Vassilev, R. Monje, A. Pavolotsky, D. Dochev, and V. Belitsky

*Proc. 17<sup>th</sup> Int. Symposium on Space Terahertz Technology* (2006)



# Contents

<b>Introduction .....</b>	<b>1</b>
<b>Technological and Scientific Background .....</b>	<b>3</b>
2.1 Superconductivity .....	3
2.2 Heterodyne Receivers for Radio Astronomy .....	5
2.2.1 Heterodyne Mixing .....	5
2.2.2 Receiver Topologies .....	6
2.3 Mixing Elements for Heterodyne Receivers .....	8
2.3.1 Frequency mixing with SIS tunnel junctions .....	8
2.3.2 Limitations of SIS Mixers .....	10
2.3.3 Frequency Mixing with Hot Electron Bolometer (HEB) .....	11
2.3.4 Limitations of HEB Mixers .....	13
<b>Studies and Development of Superconducting Components and Circuits ...</b>	<b>15</b>
3.1 Aging and Annealing of Nb/Al-AlO <sub>x</sub> /Nb Tunnel Junctions ..	15
3.1.1 Overview .....	15
3.1.2 Aging and Annealing Procedure .....	16
3.1.3 Results and Discussion .....	17
3.1.4 Summary .....	19
3.2 Superconducting IF Biasing Circuit .....	20
3.2.1 Background and Motivation .....	20
3.2.2 Circuit Design and Performance .....	21
3.2.3 Further Development .....	23
3.2.4 Summary .....	24
<b>Nb<sub>3</sub>Al High Energy-Gap Superconductor for Low-Noise THz Electronics..</b>	<b>25</b>
4.1 Overview and Motivation .....	25
4.2 Properties of Nb <sub>3</sub> Al .....	26
4.2.1 Crystal Structure and Phase Diagram .....	26
4.2.2 Nb <sub>3</sub> Al as Superconductor .....	27
4.2.3 Nb <sub>3</sub> Al Thin Films – Applications and Challenges .....	28
4.3 Fabrication and Characterization Techniques .....	28
4.3.1 Overview of Existing Deposition Techniques for Nb <sub>3</sub> Al Thin Films .....	29
4.3.2 Co-sputtering of Nb <sub>3</sub> Al and Dedicated Equipment .....	31
4.3.3 Heat Treatment and Post Annealing of Nb <sub>3</sub> Al Films .....	31
4.3.4 Characterization Techniques .....	32
4.4 Results and Discussion .....	33
4.4.1 Heteroepitaxy on Nb Seed Layers .....	33
4.4.2 Estimation of Superconducting Parameters .....	37

4.4.3	Epitaxial Growth of Nb <sub>3</sub> Al Thin Films on YSZ.....	39
4.5	Summary .....	42
<b>Towards Integrated THz Array Receivers .....</b>		<b>43</b>
5.1	Design of a Balanced Waveguide HEB Mixer.....	43
5.1.1	Mixer Layout.....	43
5.1.2	HEB Mixer on Si Beams: Motivation and Concept .....	44
5.2	RF Design and Simulations.....	46
5.1.4	Thermal Simulations .....	49
5.2	Results.....	50
5.2.1	Ultra-Thin NbN Films on Si and 3C-SiC/Si Substrates .....	50
5.2.2	HEB Devices on Si and 3C-SiC/Si Substrates .....	50
5.2.3	HEB Devices on Si Beams.....	51
5.4	Summary .....	53
<b>Future Directions and Summary of Appended Papers .....</b>		<b>55</b>
6.1	Future Directions.....	55
6.2	Summary of Appended Papers.....	56
<b>Appendix A: Crystallographic relationship between Nb<sub>3</sub>Al and Nb.....</b>		<b>59</b>
<b>Appendix B: Abbreviations and notations .....</b>		<b>61</b>
<b>Acknowledgements .....</b>		<b>63</b>
<b>References.....</b>		<b>65</b>

# Chapter 1

## Introduction

Superconducting detectors play a significant role in astrophysics and have progressed faster than any other technology from millimeter to far-infrared (IR) wavelengths. The reason for this fast evolution of superconducting detectors is the ability to provide outstanding/quantum-limited sensitivity, large array sizes and being up-to-date with the development of the fabrication technology. Hence, for more than 30 years, the research in the frequency range 30 GHz–15 THz has obtained precious information about processes such as formation of stars and planetary systems, galaxy evolution, estimation of atmospheric ingredients, dynamics of planets and comets, global monitoring, etc. [1]. In spite of being a very fascinating part of the electromagnetic spectrum, the THz range, highlighted in Fig. 1.1 still remains one of the least explored bands. Therefore, there is a continuous enormous amount of research being done in the area of millimeter and submillimeter techniques.

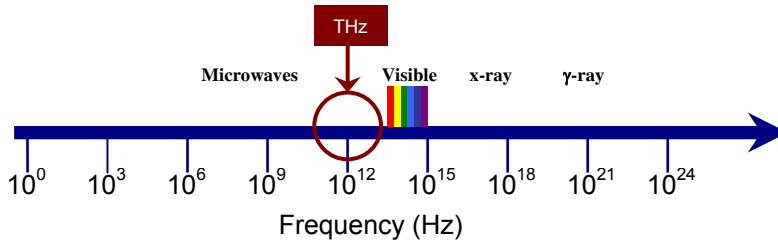


**Figure 1.1:** Schematic representation of the electromagnetic spectrum from radio to gamma rays, highlighting the THz region, which is surrounded between the microwave and infrared [2].

The space and time allocated for this work is only adequate to highlight few of the major component technologies. This thesis summarizes the work accomplished toward realization and characterization of high energy-gap superconductors, such as  $\text{Nb}_3\text{Al}$  and  $\text{NbN}$ , as well as development of novel components for low-noise THz receiver applications.

The thesis is organized as follows: *Chapter 2* provides a brief introduction to the field of superconductivity and an overview of the existing mixing technologies for radioastronomical applications, considering the most commonly employed heterodyne receiver topologies and superconducting heterodyne detectors. Next, in *Chapter 3*, systematic studies on the effects, associated with room-temperature aging and annealing of  $\text{Nb/Al-AlO}_x/\text{Nb}$  tunnel junctions are

given as part of the research on a 385-500 GHz SIS mixer for the APEX telescope. In addition, the work on the development of a novel superconducting 4-8 GHz biasing circuit for the same SIS mixer is also presented. Nb<sub>3</sub>Al superconducting material has been considered as a strong candidate for SIS mixer applications above 1 THz. Achievements on the deposited high energy-gap Nb<sub>3</sub>Al superconducting films are reported in *Chapter 4*. The films were deposited using a novel heteroepitaxial and epitaxial approach and discussion on the structural, electrical and magnetic properties is supplied. Finally, *Chapter 5* presents the ongoing work and the advancements towards HEB-based array receivers. Results on in-house deposition of ultra-thin NbN films for phonon-cooled HEB mixers as well as design and fabrication of novel layout of HEB mixer, employing SOI substrates is presented. Conclusions of the presented work, together with ideas for further developments are given in *Chapter 6*. As supplementary information, *Appendix A* shows the crystallographic relationship between Nb<sub>3</sub>Al and Nb.

# Chapter 2

## Technological and Scientific Background

### 2.1 Superconductivity

This thesis to great extent concerns thin films, devices and circuits based on superconducting materials, which are characterized by certain electrical, magnetic and other properties. Here a brief review of some of the important definitions and parameters about superconductors is made.

A superconductor can be defined as a conductor that has undergone a phase transition to a lower energy state below a transition temperature  $T_c$  in which conduction electrons form pairs, called Cooper pairs, which carry electrical current without any resistance to the flow, and which are responsible for a perfect diamagnetism and other properties [3].

Superconductors fall into two classes, type-I or type-II, depending on the sign of the surface energy for the superconductor-normal interface: type-I with a positive interface energy and type-II, with a negative interface energy [4]. A type-I superconductor exhibits two characteristic properties, namely zero DC electrical resistance and perfect diamagnetism, when it is cooled below its critical temperature,  $T_c$ . Above  $T_c$  it is a normal metal, but usually not a very good conductor. The second property of perfect diamagnetism, also called the Meissner effect, means that a magnetic field (i.e. magnetic flux) cannot exist inside the material. There is a critical magnetic field,  $H_c$ , with a property that at the temperature 0 K applied fields  $H \geq H_c$  drive the material into its normal state. Most superconducting pure metals are type-I superconductors and their critical temperature are relatively all low.

Type-II superconductors are also perfect conductors of electricity, with zero DC resistance, but with more complex magnetic properties. When the applied magnetic field is below the lower critical field,  $H_{c1}$ , it totally excludes magnetic flux. Flux is only partially excluded when the applied field is in the range  $H_{c1} < H < H_{c2}$ . For applied field  $H \geq H_{c2}$  the material becomes normal. Superconductivity in these materials can be sustained up to very magnetic fields. Type-II superconductors include some of the pure metals, such as niobium, as well as all compound and high-temperature superconductors. Devices and circuits based on Nb thin films are considered in *Chapter 3*, whereas *Chapter 4* and *Chapter 5* concern the compound superconductors  $Nb_3Al$  and  $NbN$ , respectively.

Important parameters of superconductors for practical applications include critical temperature  $T_c$ , energy gap  $\Delta$ , penetration depth  $\lambda$ , coherence length  $\zeta$ , critical fields  $H_c$ ,  $H_{c1}$  and  $H_{c2}$ , and critical current density  $J_c$ .

The energy gap  $\Delta$  of a superconductor separates the energy levels of elementary excitations and the ground state level, i.e., the energy level of the Cooper pairs, as illustrated in Fig. 2.1 [5].  $\Delta$  is directly related to the critical temperature  $T_c$  of the superconductor as [6]:

$$\Delta(0) = 1.76k_B T_c, \quad (2.1)$$

where  $k_B$  is the Boltzmann constant. The minimum energy required to break a Cooper pair and create two quasiparticle excitations is thus,  $2\Delta$ .

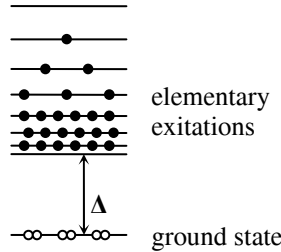


**Figure 2.1:** Energy diagram of a superconductor [5].

Another major physical parameter for any superconductor is the penetration depth,  $\lambda$ , which describes the scale of exponential decay of the magnetic field penetrating the interior of the superconductor, as shown in Fig 2.2. The London's theory defines the penetration depth as [3]:

$$\lambda_L = \left( \frac{c^2 m^*}{4\pi e^2 n_s} \right)^{1/2} \quad (2.2)$$

where  $c$  is the velocity of light,  $e$  is the charge of the electron,  $m^*$  is effective mass of the superconducting carriers and  $n_s$  is the superconductor carrier density. Practical microwave superconducting circuits require relatively short penetration depth, within few hundred nanometers at maximum, so it would not be an obstacle for fabrication by means of thin film deposition, like sputtering or evaporation. Moreover, low penetration depth is essential to reduce the parasitic inductance within the superconducting circuits.

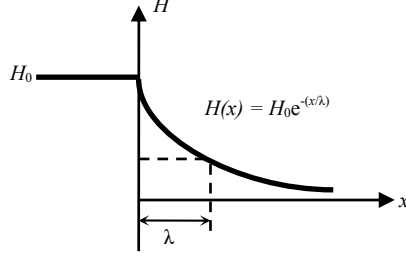


**Figure 2.2:** Schematic representation of the magnetic field decay in the interior of the superconductor.

The second characteristic length of a superconductor is the coherence length  $\xi$  and it defines the intrinsic nonlocality of the superconducting state, i.e., the distance at which  $n_s$  changes significantly. In pure superconductors far below  $T_c$ ,  $\xi(T) \approx \xi_0$ , and it is defined as [6]:

$$\xi_0 = \frac{\hbar v_F}{2\Delta(0)}, \quad (2.3)$$

where  $\hbar$  is the Planck's constant and  $v_F$  is the Fermi velocity in the material. The coherence length gives also a scale of the so-called superconducting proximity effect, in which superconductivity is induced in the normal metal in contact with superconductor, and vice versa, superconductivity gets suppressed in contact with a normal metal [4]. In addition, the characteristic lengths  $\lambda$  and  $\xi$  allow a unique description of the surface impedance in the normal and superconducting state [6].

## 2.2 Heterodyne Receivers for Radio Astronomy

### 2.2.1 Heterodyne Mixing

Coherent receiver is of great importance for radio astronomy due to the possibility to exploit very high spectral resolution, required for fine-structure atomic and molecular spectroscopy. The coherency of heterodyne mixing process is based on the important property of preservation of both amplitude and phase information carried by the incoming signal. The function of a heterodyne receiver is to “mix” a weak incoming signal at frequency ( $f_s$ ) with a large-amplitude local oscillator (LO) at  $f_{LO}$ , in order to produce much lower intermediate frequency (IF) output at  $f_{IF}$ , suitable for signal post detection processing. By keeping the IF fixed and by varying the LO, it is possible to tune the receiver along a wide band of incoming signal frequencies. This principle is extensively used in various applications such as satellite communications, radars, mobile phones, etc. A basic schematic of a heterodyne receiver is shown in Fig. 2.3. Here the frequency down conversion is carried out by a mixer, which is a nonlinear element. An overview of mixing elements used for high resolution THz spectroscopy is provided in *Section 2.3*.

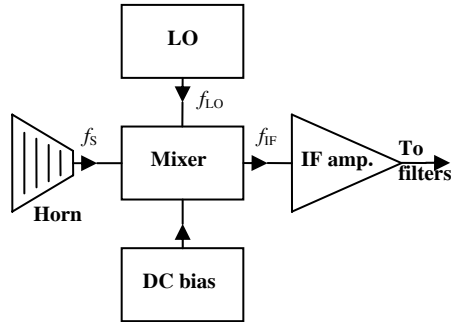


**Figure 2.3:** Block diagram of a heterodyne receiver [7].

## 2.2.2 Receiver Topologies

In reality, the mixer will produce the same IF for frequencies ( $f_s = f_{LO} - f_{IF}$ ) or ( $f_s = f_{LO} + f_{IF}$ ) [8], Fig. 2.4. The sum and difference frequencies at ( $f_{LO} \pm f_{IF}$ ) are called the sidebands of the carrier frequency ( $f_{LO}$ ), with ( $f_{LO} + f_{IF}$ ) being the upper sideband (USB), and ( $f_{LO} - f_{IF}$ ) being the lower sideband (LSB). In the USB case, the desired IF output in a receiver is the difference frequency, ( $f_{IF} = f_s - f_{LO}$ ). However, a received input signal at frequency ( $f_{IM} = f_{LO} - f_{IF}$ ), called an image frequency, will be also down converted to the same IF, so the IF will be superposition of both signal and image frequencies.

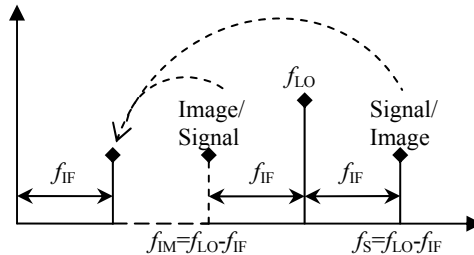


**Figure 2.4:** Location of the signal, LO, IF and image frequencies in a frequency down-conversion.

A mixer that responds simultaneously to both the LSB and USB is called a double sideband (DSB) mixer. This property is used, for example in continuum radiometry, where broadband sources are typically measured. The DSB mode is in most cases undesirable since the unnecessary sideband can create interfering signals, which cause line confusion and bring additional (atmospheric) noise, etc. and hence, degrade the signal-to-noise ratio.

In order to realize more sensitive instruments for spectroscopic observations the unwanted sideband must be suppressed. This is achieved in a so called single sideband (SSB) scheme. A standard way to do this is by placing an image-rejection filter at the signal input. For practical instruments the sideband rejection ratio is required to be better than 10 dB. Nevertheless, employing an additional filter at the mixer input in a radioastronomical receiver will lead to increased

losses, consequently – higher receiver noise, a necessity for tuning and more complex optics design.

More sophisticated approach to separate the upper and lower sidebands at IF is realized in sideband separating (2SB) mixers, as shown in Fig. 2.5. For this purpose two individual DSB mixers are employed in a quadrature scheme with phase cancellation at IF. This implies that RF and IF quadrature hybrids are used. Perfect sideband cancellation occurs when the RF and LO signals are divided equally with accurate phase. Termination of the image bands from both DSB mixers occurs at the idle port of the RF hybrid.

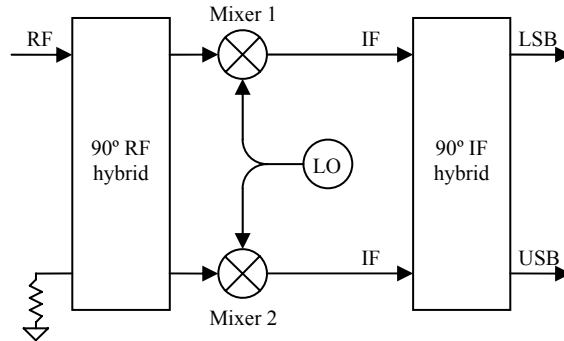


**Figure 2.5:** Block diagram of a sideband separating (2SB) mixer.

A receiver with a balanced scheme, as depicted in Fig. 2.6, has an advantage over single-ended mixer configuration due the reduced thermal and AM noise from the LO and the more effective way of using the available LO power [9]. The balanced type of topology requires a  $90^\circ$  or  $180^\circ$  input hybrid circuitry, which can supply with equal amount of LO and RF power two identical DSB mixers, where the IF outputs are combined via IF hybrid. Balanced mixers with  $180^\circ$  input hybrids exhibit superior LO-RF isolation properties and intermodulation (IM) product suppression as compared to  $90^\circ$  hybrid based balanced mixers. However, for mm- and sub-millimeter waveguide mixer applications, the  $90^\circ$  balanced mixers are usually preferred since they are more compact and easier to fabricate and most importantly, provide broad RF band.

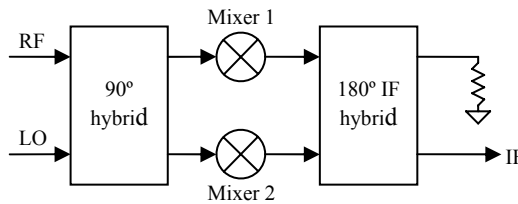


**Figure 2.6:** Block diagram of a  $90^\circ$  balanced mixer.

## 2.3 Mixing Elements for Heterodyne Receivers

The key component of every heterodyne receiver is the mixing element. In the terahertz range heterodyne receivers typically employ as nonlinear device Schottky diodes, superconductor-insulator-superconductor (SIS) tunnel junctions or hot electron bolometers (HEB). Before the appearance of SIS and HEB mixers, heterodyne receivers for atmospheric and radioastronomical observations were generally based on Schottky-diode mixers. However, along with the relatively high receiver noise temperature for Schottky-diode mixers, compared to the SIS and HEB technologies, as shown in Fig. 2.7 [1], another vital limitation is the high LO power requirements ( $\sim 0.5$  mW) [10]. Higher sensitivity THz detectors based on SIS and HEB devices, rely on cryogenic cooling and require much lower LO power than Schottky mixers. In the following section, the basic operational principles of mixers based on SIS tunnel junction and HEB are briefly described.

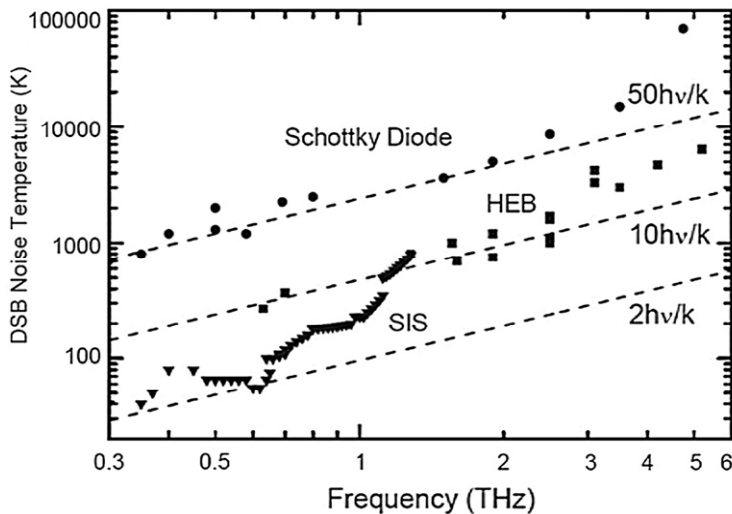


**Figure 2.7:** State-of-the-art noise performance of Schottky diode (circles), SIS (triangles) and HEB mixers (squares). Reproduced from [1].

### 2.3.1 Frequency mixing with SIS tunnel junctions

Superconductor-insulator-superconductor (SIS) tunnel junctions are quantum mechanical devices consisting of two superconductors separated by a very thin insulator ( $\sim 1$  nm), as illustrated in Fig. 2.8. Besides tunneling of Cooper pairs through the insulator, known also as Josephson effect, a finite voltage across the junction can “dissociate” pairs and create a current of single electrons, i.e., a quasiparticle current. The current-voltage characteristics of the quasiparticle current are extremely nonlinear and can be used for frequency mixing. The operation of a SIS mixer is based on the principle of photon-assisted tunneling [11] by quasiparticles across a thin barrier [7].

The superconductors (S) on both on both sides of the tunnel barrier (I) at temperature  $T = 0$  K are in their ground state, i.e. the electrons are bound into Cooper pairs. The minimum energy required for excitation of a Cooper pair for each electrode above the ground state and thus, producing two single-particle excitations is therefore  $2\Delta$ . This breaking energy is also known as superconducting energy gap. At zero bias voltage the Cooper pair can still tunnel through the junction producing a super current,  $I_c$ . Increasing the applied voltage to the value of the gap voltage,  $V_0 = 2\Delta/e$ , an onset of the quasiparticle tunneling takes place. At this potential a single electron is able to tunnel through the barrier leaving an un-paired quasiparticle behind.

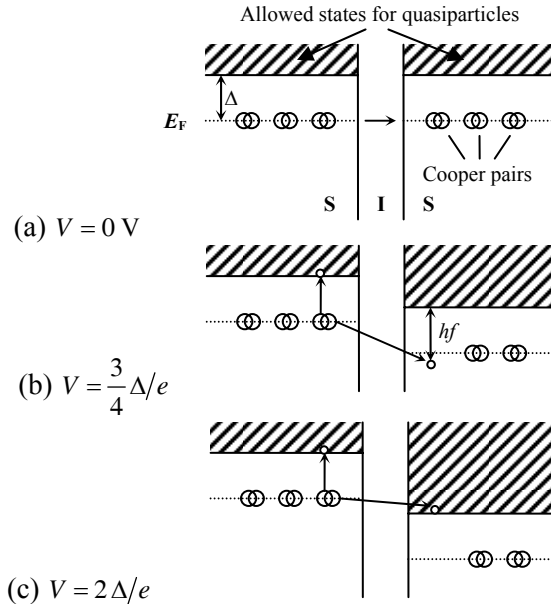


**Figure 2.8:** Quasiparticle tunneling for a symmetric junction [12].

When a SIS tunnel junction is irradiated with microwave radiation of frequency  $f$ , the absorption of  $n$  quanta inside the barrier can provide enough energy to open this channel for quasiparticle tunneling when  $eV_0 = 2\Delta - nhf$ . This phenomena is called photon-assisted tunneling and as a result constant-current steps separated by voltage of  $\delta V = hf/e$  appear on the quasiparticle branch (below the DC onset) of its I-V characteristics, as shown in Fig 2.9. It has to be noted that the absorption probability decreases rapidly as the photon number  $n$  increases.

When a local oscillator signal is applied to the biased SIS junction it will modulate the DC I-V curve in such way that the LO power will determine the number of photon steps. Highest sensitivity of the mixer is usually achieved when it is biased in the middle of the first photon step below the gap voltage.

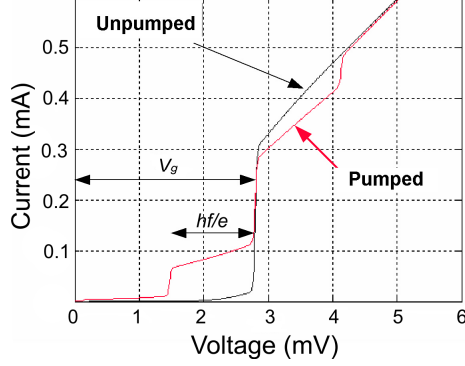


**Figure 2.9:** Current-voltage characteristics of Nb/Al-AlO<sub>x</sub>/Nb SIS tunnel junction with and without applied LO power.

Along with the quasiparticle current a portion of Cooper pair current also exists, known as Josephson current, which causes instability and additional noise in the mixer. In the I-V characteristics the contribution from the Josephson current appears as current steps at discrete voltages  $n\hbar f_{LO}/2e$ , also called Shapiro steps. In order to suppress the Josephson current, typically a magnetic field is applied across the junction. This is based on the fact that the critical current  $I_c$  is a function of the magnetic field flux  $\Phi$  passing through the barrier region as:

$$I_c = I_c(0) \left| \frac{\sin(x)}{x} \right|, x = \frac{\pi\Phi}{\Phi_0} \quad (2.4)$$

Hence, the Josephson current disappears for a value of the applied magnetic flux  $\Phi$  equal to  $n\Phi_0$ , where  $\Phi_0$  is the magnetic flux quanta. The value of the corresponding magnetic field,  $B$ , needed for suppression of the Josephson current depends on the geometrical dimension on the SIS junction,  $L$ , the barrier thickness,  $d$ , and the magnetic penetration depth,  $\lambda$ :

$$B = \frac{\Phi_0}{L(d + 2\lambda)} \quad (2.5)$$

Naturally, depending on the shape of the SIS junction the modulation of the critical current in eq.(2.4) will have different pattern, etc.

### 2.3.2 Limitations of SIS Mixers

For ambient temperatures well below the critical temperature, the SIS devices reach a natural frequency limit at approximately twice the superconducting energy gap,  $2\Delta$ . This upper operating frequency is dependent upon the tunnel junction material composition. For most common SIS tunnel junctions, Nb/Al-AlO<sub>x</sub>/Nb with  $T_c = 9.3$  K, this frequency approaches near 1350 GHz. In addition,

the high intrinsic capacitance of the SIS junctions requires an additional tuning circuit which should compensate for the SIS capacitance and perform impedance transformation. The losses in the superconducting RF matching circuit cause a drastic increase of the mixer noise temperature at frequencies above the gap frequency. Hence, for Nb-based tuning circuits the corresponding upper frequency limit is about 700 GHz.

This issue is typically addressed by using superconducting materials with higher energy-gap than niobium which give the possibility to exploit higher frequencies. Advances towards higher frequency of operation of the SIS mixers were previously made using materials such as NbN ( $T_{c,NbN} = 16$  K) and NbTiN ( $T_{c,NbTiN} = 17$  K) and were demonstrated to be useful materials for SIS junctions and embedding circuitry, respectively [14]. Although NbN and NbTiN showed significant improvement, acceptable tunnel junctions based on these materials have yet to be formed.

A large part of the work described in this thesis has been devoted to the development of another wide-gap superconducting material such as Nb<sub>3</sub>Al ( $\Delta = 3.04$  meV) as a promising material for tuning circuitry as well as tunnel junctions. *Chapter 4* presents the results obtained towards realizing reproducible Nb<sub>3</sub>Al films with lowest possible resistivity and highest possible transition temperature.

Instability of the junctions is an obvious drawback when considering practical and commercial applications. Recently, more and more sensitive and higher-frequency receivers based on SIS mixers are being deployed on ground-based single-dish telescopes. Large-scale projects, such as ALMA, play an important role in developing this field. For example, the lifetime of the ALMA project is considered to be at least 20 years and this requires extremely reliable and stable Nb/Al-AIO<sub>x</sub>/Nb tunnel junctions. These components are meant to operate under extreme conditions, repeated thermal cycling between room and LHe temperature, long-term storage at room temperature, etc. Therefore, any variation of the intrinsic junction parameters, e.g. the normal-state-resistance, will detune the mixer and thus, degrade the performance of the instrument. *Chapter 3* in this thesis gives an insight into behaviour of a large number of high-quality tunnel junctions subjected to long-term room temperature aging. This study also provides a reproducible scheme for stabilization of the tunnel junctions by means of thermal annealing at moderate temperature.

### 2.3.3 Frequency Mixing with Hot Electron Bolometer (HEB)

An alternative to SIS mixers for high resolution spectrometry beyond 1 THz is the superconducting hot electron bolometer (HEB) mixer. Since their introduction in 1990 [15], the HEB devices have evolved so far into practically usable mixing-elements at frequency as high as 5.3 THz [16]. The major advantages of this type of mixers are: 1) unlimited RF frequency bandwidth; 2) no necessity for external magnetic field; 3) no additional tuning circuitry is needed due to the real device impedance.

The HEB device is a strip of thin superconducting film (Nb, NbN, NbTiN, Al, etc.) made on a dielectric substrate between two contacts, Fig.2.10. The

superconducting bridge has typically a width up to several micrometers and a length up to few hundred nanometers. In practice, the device is cooled down below its critical temperature and brought to its operating regime by applying sufficient DC bias and radiation power from a local oscillator. Since the electrons in the film are only weakly coupled to the phonons, the absorbed energy is transferred mainly to the electron gas. This condition brings the electrons to a temperature  $T_e$ , higher than the phonon temperature  $T_{ph}$ . In the vicinity of  $T_c$ , the superconducting energy gap is strongly suppressed resulting in a low-concentration of Cooper pairs. At these conditions, small changes in the absorbed photon power will induce large variation in the resistance and, thus, alter the voltage across the bolometer. The superposition of a strong LO signal and a weak RF signal causes a time-averaged heating fluctuations at the difference (intermediate) frequency  $f_{IF} = |f_{LO} - f_{RF}|$ .

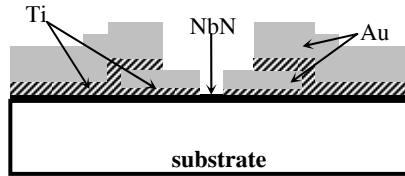


**Figure 2.10:** A cross-sectional view of an NbN HEB device.

The mixer's intrinsic IF bandwidth is determined by the speed of the electron relaxation process, which is illustrated in Fig 2.11. The electron-electron interaction time,  $\tau_{e-e} \approx (R_{\square} T_e)^{-1}$  [17], is much shorter than the electron-phonon interaction time,  $\tau_{e-ph} \approx (T_e)^{-3/2}$  [18]. This condition ensures that during the time  $\tau_{e-e}$  the heating of the lattice will be negligible, and at any frequency the energy of the absorbed energy is redistributed effectively among the electrons [19]. Cooling of the "hot" electrons is achieved either by creating phonons, which "escape" into the substrate, or by out-diffusion of electrons into the contact pads. The former process is known as phonon cooling, whereas the latter cooling mechanism is referred as diffusion cooling [20]. Part of this thesis deals with development of phonon-cooled type HEB devices based on ultra-thin NbN films. Therefore, the attention will be focused on the phonon-cooling mechanism and therefore, diffusion cooled will not be discussed.

Phonon-cooling, as depicted in Fig. 2.11, implies that non-equilibrium phonons generated in the strip by electrons should get away into the substrate as fast as possible so no energy is transferred back to the electrons. The escape time of phonons into the substrate,  $\tau_{esc}$ , is given by [21]:

$$\tau_{esc} \approx 4d / \alpha u, \quad (2.6)$$

where  $d$  is the film thickness,  $u$  is the sound velocity in the film and  $\alpha$  represents the acoustic matching between the film and the substrate. Equation (2.6) means that the film has to be made sufficiently thin, so the

phonons escape time becomes shorter than the phonon-electron interaction time,  $\tau_{\text{ph-e}}$ . Moreover, making the bridge narrow enough, the backflow of phonons from the substrate to the films will be reduced [22].

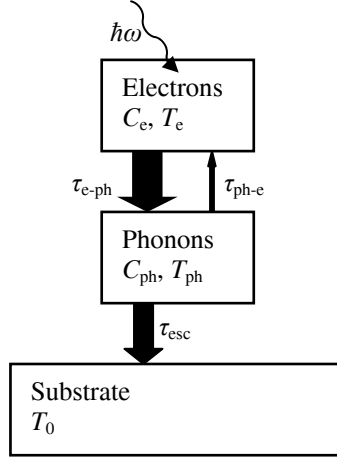


**Figure 2.11:** Electron relaxation process in NbN HEB mixer. [22]. Here  $C_e$  and  $C_{\text{ph}}$  are the electron and phonon specific heats, respectively.  $T_0$  is the ambient (substrate) temperature, whereas  $T_e$  and  $T_{\text{ph}}$  are the electron and phonon effective temperatures, respectively. For a 3.5 nm NbN film on sapphire:  $\tau_{\text{e-e}} = 6.5$  ps,  $\tau_{\text{e-ph}} = 10$  ps and  $\tau_{\text{esc}} = 38$  ps [23].

The intrinsic IF bandwidth of the HEB mixer is determined mainly by the combination of  $\tau_{\text{e-ph}}$  and  $\tau_{\text{esc}}$ . Hence, the total electron relaxation time,  $\tau_\theta$ , which determines how fast the temperature of the bolometer can follow the changes in the radiation power, is defined as [21]:

$$\tau_\theta = \tau_{\text{e-ph}} + \tau_{\text{esc}} C_e / C_{\text{ph}}, \quad (2.7)$$

where  $C_e$  and  $C_{\text{ph}}$  are the electron and phonon specific heat, respectively.

### 2.3.4 Limitations of HEB Mixers

Phonon-cooled HEB mixers suffer from limited IF bandwidth. The cause for the narrow IF bandwidth, typically between 2.5–5 GHz, is the large thermal time constants associated with the cooling mechanism of the hot electrons. The narrow IF bandwidth in HEB mixers limits the astronomical observations of galactic sources due to limited velocity coverage (Doppler shift) at THz frequencies [24]. In the context of increasing the IF bandwidth of HEB mixers, *Chapter 5* provides studies on HEB devices based on epitaxially grown ultra-thin NbN film on 3C-SiC/Si substrate with enhanced critical temperature above 11 K. The fabricated devices showed reliable characteristics and strong potential for further use with HEB THz mixers.

Reducing the LO power consumption of the HEB mixer by decreasing the device size can induce a direct detection problem. This often occurs when the absorbed RF power is in the same order as the absorbed LO plus DC power. The direct detection results in poorer stability characteristics of the mixer. The change of the mixer bias current due to direct detection alters the optimal operating point and produces standing waves between the mixer and the low-noise amplifier (LNA). However, the issue with direct detection in HEB mixers can be eliminated by utilizing a waveguide-based design, thus reducing the passband. The waveguide approach gives also a possibility to use a corrugated horn antenna, which provides well defined beam pattern at the receiver input. *Chapter 5* presents a novel waveguide-based HEB mixer design which in combination with recent advancement of THz waveguide fabrication [25] could extend the use of waveguide-based mixers beyond 2 THz.

An important issue in HEB receivers is the reduction of the thermal and amplitude modulation (AM) noise from the local oscillator. A way to get around this concern is to employ a HEB-based mixer with a balanced scheme, which exhibits superior performance than commonly used single-ended mixers [26]. However, balanced-type HEB waveguide mixers employ two identical mixing elements fabricated on extremely fragile quartz substrate which complicates the handling and assembly. *Chapter 5* presents a novel integration scheme for waveguide-based HEB mixer on thin silicon beam employing standard SOI technology. The demonstrated integration concept has a strong potential to be utilized in heterodyne array receivers above 1 THz.

## Chapter 3

# Studies and Development of Superconducting Components and Circuits

### 3.1 Aging and Annealing of Nb/Al-AlO<sub>x</sub>/Nb Tunnel Junctions

The aging properties of the active components are of high importance for mm- and submm-wave receiver applications. Long-term storage at room temperature, repeated thermal cycling and annealing at moderate temperatures could lead to a change of the characteristics of the mixing element and cause large spreads in its critical parameters. The variation of the properties of Nb/Al-AlO<sub>x</sub>/Nb tunnel junctions under room temperature aging and annealing at elevated temperatures has been of interest in many studies [27-34]. Along with the commonly agreed trends and understanding, there are experimental facts, which cannot be still explained within the suggested processes and mechanisms. The following section as well as *Paper B* and *Paper C*, describe the experimental procedure on long-term aging at room temperature and repeated annealing of high-quality Nb/Al-AlO<sub>x</sub>/Nb tunnel junctions. A discussion and interpretation of the experimental results are presented in terms of structural ordering in the vicinity of the tunnel barrier.

#### 3.1.1 Overview

By the beginning of 1980s radio telescope heterodyne receivers have been largely used lead alloy tunnel junctions [7]. A common problem with the Pb-alloy junctions was the lack of stability upon thermal cycling and storage at room temperature. Nb/NbO<sub>x</sub>/Nb and Nb/NbO<sub>x</sub>/Pb junctions could benefit from the higher critical temperature of Nb ( $T_c = 9.3$  K) but, in a similar manner, were not capable to provide the desired cycling and storage stability. In addition, NbO<sub>x</sub> tunnel barriers have poor tunneling properties and high dielectric constant [13]. Together with Nb<sub>2</sub>O<sub>5</sub>, various suboxides, such as NbO and NbO<sub>2</sub>, are also present in the barrier region, thus making the barrier itself inhomogeneous. On the other hand, AlO<sub>x</sub> tunnel barriers in Al/AlO<sub>x</sub>/Al junctions were known to possess extremely high quality - low leakage and excellent thermal cycling stability. However, the low critical temperature of Al, respectively a low superconducting gap, makes these junctions not useful for practical applications.

In comparison to all abovementioned tunnel junctions, Nb/Al-AIO<sub>x</sub>/Nb tunnel junctions were found [35] to combine the advantages of high superconducting gap of Nb with the high-quality AlO<sub>x</sub> tunnel barrier: 1) small leakage current in the subgap region; 2) a sharply defined gap voltage; 3) excellent stability, both against long term storage and thermal cycles; 4) excellent stability, both against long term storage and thermal cycles; 4) controllability of the critical current [36]. The Nb/Al-AIO<sub>x</sub>/Nb junction is composed of four stacked layers: a base Nb layer, a thin Al layer, an AlO<sub>x</sub> barrier, and a top Nb layer as shown in the HRTEM image in Fig. 3.1. The success of the Nb/Al-AIO<sub>x</sub>/Nb is based on the high-quality ultra-thin (~10 Å) AlO<sub>x</sub> tunnel barrier due to the good planarizing properties of the underlying Al layer. It was found that a very thin (a few nm) layer of Al completely covers the Nb surface and hence, create a continuous surface free of pinholes [37]. To date, most of the radioastronomical receivers incorporate Nb/Al-AIO<sub>x</sub>/Nb tunnel junctions. The fabrication methodology for Nb/Al-AIO<sub>x</sub>/Nb junctions has been presented by Gurvitch *et al.* [35] almost 30 years ago and the technique has largely remained unchanged.

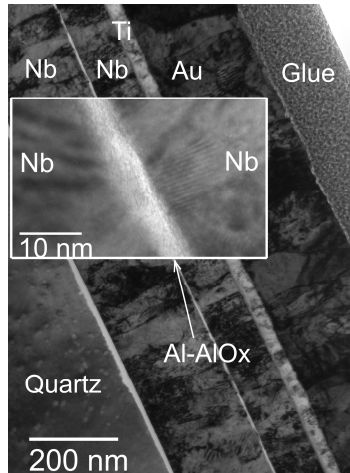


**Figure 3.1:** Cross-sectional HRTEM micrograph of Nb/Al-AIO<sub>x</sub>/Nb trilayer deposited on a quartz substrate with a close-up view of the tunnel barrier.

### 3.1.2 Aging and Annealing Procedure

Room temperature aging data was collected from more than 100 high-quality SIS junctions, which were stored for more than one year at standard conditions (air-conditioned laboratory room with controlled humidity and temperature). The tunnel junctions used in this study were produced at different stages of the development of a SIS mixer chip, used for the Band 3 (385-500 GHz) SHEFI receiver at the APEX telescope [38, 39]. The variation of the normal-state resistance ( $R_n$ ) and the subgap-to-normal resistance ratio  $R_g/R_n$  of the Nb/Al-AIO<sub>x</sub>/Nb tunnel junctions were extracted from the measured current-voltage characteristics, as illustrated in Fig. 3.2. No additional measures were taken to protect the wafers from atmospheric exposure during the storage period. After

performing the long-term room temperature aging, the same junctions were subjected to a thermal annealing. The heat treatment of the samples has been carried out by placing them onto a hot plate with the temperature set at 120°C for 1 hour in a cleanroom environment with relative humidity of  $42 \pm 2\%$ . After the annealing, the junction I-V characteristics were measured in a dipstick in LHe at 4.2 K. The same procedure was repeated several times with a temperature increment of 10°C up to a temperature as high as 250°C, keeping the same annealing time. Since the temperature range of the hotplate was limited to 200°C, the annealing within the temperature range 200-250°C was done in an oven by placing the wafer onto a preheated massive metal wafer holder in order to have temperature ramping conditions similar to that of the hotplate.

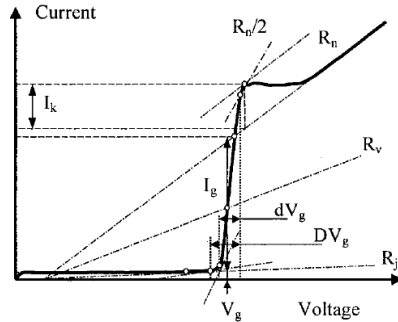


**Figure 3.2:** Typical current-voltage characteristic of an SIS tunnel junction and its intrinsic parameters. Here  $R_n$  is the normal state resistance;  $R_j$  – subgap resistance, estimated at 1.7 mV,  $V_g$  – gap voltage;  $R_v$  – line for definition of the gap voltage;  $I_g$  – current rise at the gap voltage;  $I_k$  – current, characterizing the knee structure just above the gap;  $dV_g$  – gap smearing using  $R_n/2$  criterion;  $DV_g$  – gap smearing using  $R_j/2$  criterion [40].

### 3.1.3 Results and Discussion

It was found that the value of the normal-state resistance of the junctions noticeably decreases after the long room temperature aging as shown in Fig. 3.3a. Similar decrease in  $R_n$  has been also observed by other research groups [41]. Moreover, the aging does not have just a simple effect of reducing the normal-state resistance. In fact, the subgap resistance  $R_j$  tends to increase/improve, as shown in Fig. 3.3b. This interesting result has neither been observed for Nb/Al- $\text{AlO}_x$ /Nb tunnel junctions nor has received an adequate attention. It is known that tunnel barriers fabricated by thermal oxidation, like in this study, result in an oxide layer where atoms are not in their global equilibrium positions [42]. Therefore, the decrease of  $R_n$  could be a result of the structural ordering in the  $\text{AlO}_x$  layer, which translates to reduction of the tunnel barrier thickness [43, 44]. The effect of increased subgap resistance  $R_j$ , on the other hand, might be attributed to eventual removal of additional conduction paths, associated with barrier imperfections. Hence, the “leakage” component of the sub-gap current decreases, i.e., the quality of the tunnel barrier improves. According to Fig. 3.3b, the effect of aging on  $R_j$  is observable at a time scale much shorter than that for  $R_n$ . Moreover, this process is dependent on the junction size, i.e., smaller

junctions, like these shown in Fig. 3.3b, exhibit much more pronounced change in  $R_j$  than the bigger ones.

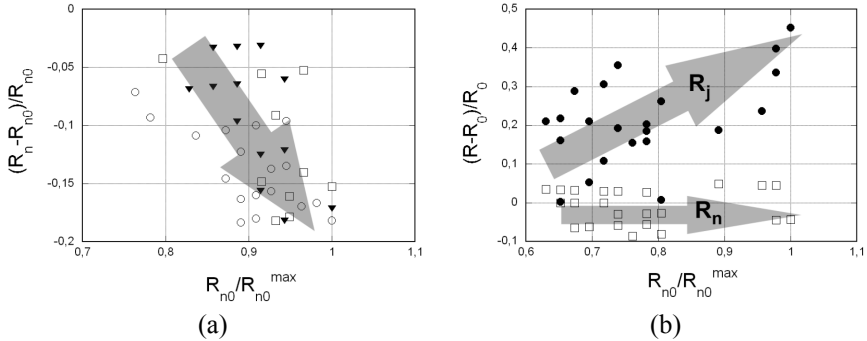


**Figure 3.3:** (a) Relative change of the normalized normal-state resistance after room temperature aging. The average aging time for all wafers (R5, R6, R7 and R8) is 17 months. (b) Relative change of the subgap and normal-state resistance for wafer D1 after 63 days of aging at room temperature. The measured parameters are normalized to the initial values right after fabrication.

Figure 3.4 shows the change on the  $R_n$  and  $R_j/R_n$  ratio normalized to their initial values after repeated annealing steps. Up to temperature of 150°C, a noticeable increase in the junction quality was observed, followed by a quick drop of the  $R_j/R_n$  ratio for higher annealing temperatures. The data is representative for junctions with different area size  $A$  in the measured batches, namely R5, R6, R7, R8 ( $A = 3 \mu\text{m}^2$ ) and D1 ( $A = 2 \mu\text{m}^2$ ). The results presented here on annealing of Nb/Al-AIO<sub>x</sub>/Nb junctions are in line with earlier studies [30, 32], where the  $R_n$  increase at moderate annealing temperature has also been observed.

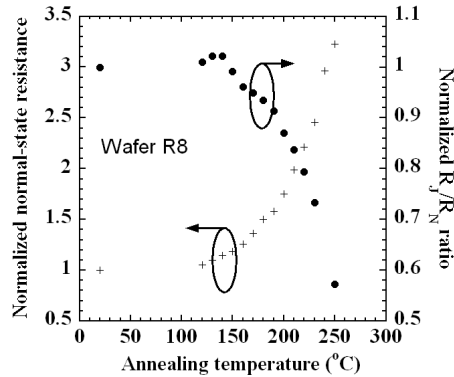


**Figure 3.4:** Normalized normal-state resistance and  $R_j/R_n$  ratio as a function of the annealing temperature. Data points are representative for wafers R5, R6, R7, R8 and D1.

For newly fabricated junctions, like those on wafer D1, the most dramatic change in the junction parameters occurred during the first 2 weeks after the fabrication. Wafer D1 was characterized directly after its completion and then left exposed to short-term aging at room temperature for two weeks as the junctions'

parameters were monitored on a weekly basis. Then the wafer was subjected to subsequent annealing, as for each annealing temperature a short-term aging up to 2 weeks was performed. The results from this experiment are presented in Fig. 3.5a. Interestingly, stabilization of the junction parameters after certain aging period was noted, in line with the reported results in [41].

Despite having nominally the same device processing, an aging history effect of the junction-to-junction lifetime persistence during the annealing process was found, as shown in Fig. 3.5b. Tunnel junctions from wafers that have been subjected to the long-term storage have comparatively longer lifetimes than junctions that were annealed shortly after fabrication. This behaviour might be attributed to diffusion ordering in the  $\text{AlO}_x$ . This process, in principle, takes far more time than stress relaxation of the Al layer. Aging at room temperature causes a deformation rate, which is slower, than annealing at elevated temperature does. So, diffusion ordering in  $\text{AlO}_x$  has better chance to catch up. Therefore, pre-aged junctions manage to sustain higher annealing temperatures than newly fabricated junctions. On the other hand, in “fresh” junctions subjected to immediate annealing treatment, the  $\text{AlO}_x$  layer cannot follow the deformation in the Al layer and eventually breaks up.

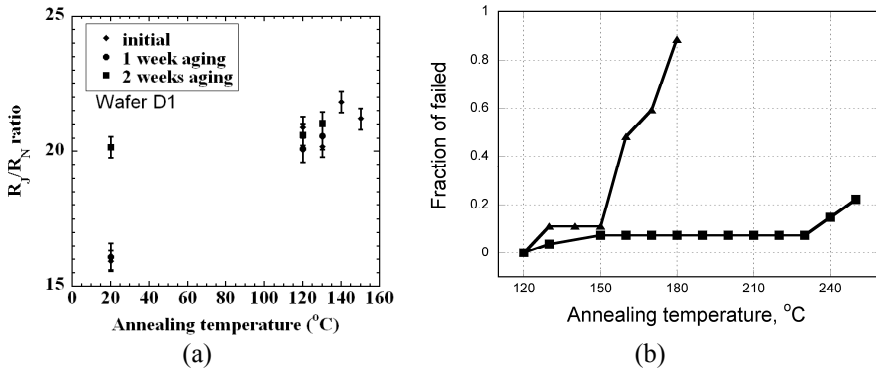


**Figure 3.5:** (a) Quality evolution/stabilization of the newly fabricated tunnel junctions subjected to a short room temperature aging and subsequent annealing. (b) Lifetime comparison between long-term aged (squares) and short-term aged (triangles) junctions after annealing.

### 3.1.4 Summary

This section presented the studies on room temperature aging and annealing behaviour of high-quality Nb/Al- $\text{AlO}_x$ /Nb tunnel junctions. A noticeable reduction of the normal state resistance,  $R_n$ , and increased subgap resistance,  $R_j$ , was observed as a result of the conducted experiments. It has been noticed that the value of  $R_j$  changes relatively quicker than that of  $R_n$ . This effect has been even more pronounced when annealing newly processed junction at moderate temperatures up to 200°C. The exhibited changes in junctions’ performance could be attributed to structural ordering/reconstruction of the tunnel barrier which happens in much longer time scale than the intrinsic stress relaxation processes in the Al layer.

## 3.2 Superconducting IF Biasing Circuit

Apart from the mixing element in SIS receivers, i.e. the SIS tunnel junction, there are number of components which are vital for the performance of the instrument. This section, as well as *Paper C*, present a design, implementation and performance of a superconducting IF biasing circuit for the frequency range 4-8 GHz used in a 385-500 GHz SIS DSB mixer installed at the APEX telescope.

### 3.2.1 Background and Motivation

An SIS tunnel junction with its RF tuning circuitry produces output an IF impedance different from the conventional  $50\ \Omega$  of the IF chain. Additionally, to obtain stable mixer operation the active component's output has to be terminated to an impedance, which provides optimum matching conditions [45]. This does not immediately imply a conjugate matching as it will cause instability of the mixer. A good trade-off between mixer gain and output reflection coefficient is achieved by termination to a real impedance with a value of about two times the normal state resistance (while the SIS capacitive component can be tuned inductively) [46]. The low real part of the complex IF impedance, e.g.  $10\text{-}20\ \Omega$ , reduces the Q factor of the resonant circuit and thus, makes the mixer less IF frequency dependent [47]. Certainly, these conditions require an additional matching network to transform the  $50\ \Omega$  of the IF chain to about  $10\text{-}20\ \Omega$  to the mixer-chip IF output.

The IF output of the mixer is also used for supplying DC bias. Hence, the IF matching circuitry has to act as a bias-T circuit. To keep the physical size small, the matching circuit and bias-T are usually merged and integrated in the mixer block [48, 49]. The bias-T decouples the IF output from the DC signal through a DC-blocking capacitor connected in series. A very common solution for the DC block is to employ a surface-mount capacitor. However, a major concern of employing the lumped element is the limited bandwidth and the parasitic resonances at higher frequencies. Moreover, mechanical stability of the soldered component during repeated thermal cycling down to cryogenic temperatures is also of crucial importance.

A way to get around these problems is to use entirely planar structure, such as, e.g., a directional coupler employing parallel-coupled suspended microstrip line, which also acts as a band-pass filter, as proposed by Kooi *et al.* [50]. However, this solution requires a cavity for the suspended microstrip section, which greatly complicates manufacturing and assembly.

An alternative design of a compact and entirely planar IF circuitry was developed, thus, combining a high-ratio impedance transformer and bias-T. Since the operating temperature of the circuit is 4 K, it is convenient to use a superconducting material, e.g. Nb, as a metallization for strip and ground conductors. In comparison to the normal-metal equivalent, this technique provides additional advantage such as the absence of IF conduction losses and no series DC resistance. Moreover, for a superconductor, such as Nb, the high-frequency "skin depth" is simply the London penetration depth,  $\lambda_L$  [4] and independent on frequency. Therefore, the thickness of the superconductor lines is

required to be  $\sim 3\lambda_L$ , i.e., about 6-7 times smaller than for the case of normal metal at the same frequency band. This allows for high accuracy of the microstrip lines, which are defined by a standard photolithographic process.

### 3.2.2 Circuit Design and Performance

The required bandwidth of 4 GHz of the impedance transformer can be obtained by using two quarter-wave sections. In addition, a planar equivalent of the DC blocking capacitor will require an extra quarter-wave section, resulting in too large circuit dimensions. Open circuited interdigital sections have been used for applications as DC blocks because of their improved performance at higher frequencies as compared to lumped capacitors [51]. Furthermore, the couple line technology provides not only large bandwidth but also impedance transform function. Therefore, the second section of the impedance transformer is implemented as a three-coupled microstrip line, which simultaneously serves as a DC-blocking capacitor. As a result, the circuit layout becomes significantly more compact and relies exclusively on planar microstrip components. Figure 3.6 shows schematically the layout of the IF circuitry.

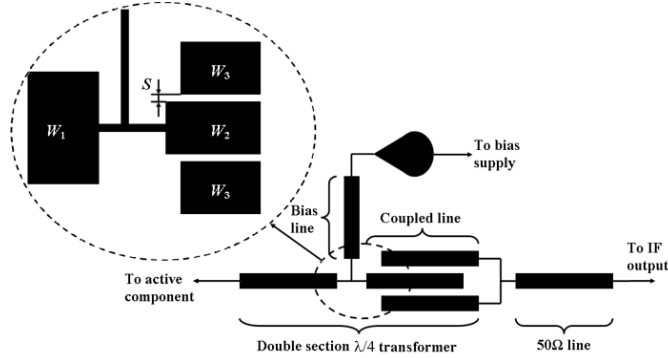


**Figure 3.6:** Schematic diagram of the IF biasing circuit.  $W_1 = 1110 \mu\text{m}$ ,  $W_2 = 170 \mu\text{m}$ ,  $W_3 = 20 \mu\text{m}$  and the spacing,  $S$ , of the coupled lines is  $30 \mu\text{m}$ .

The circuit was optimized using Agilent ADS [52] and verified by the full-wave simulator EMDS [53] based on finite element method (FEM). Limited to the particular application for the IF circuitry for SIS mixer, it is sufficient to have -10 dB return loss across the band. Simulation results are shown in Fig. 3.7. The return loss is better than -10 dB for the whole band and the insertion loss is lower than 0.3 dB within 4 to 8 GHz.

The circuitry employs superconducting metal, niobium. The Nb film is deposited by DC magnetron sputtering. The possibility of using thin superconducting films with photolithographic process offers the advantage of more relaxed design parameters of the coupled microstrip line. The 300 nm ( $\sim 3\lambda_L(\text{Nb})$ ) thick sputtered niobium layer facilitates fabrication of the narrow spacing in the three-coupled microstrip line structure and simultaneously maintain the desired capacitance of the DC-block. The circuit was fabricated on a 0.250 mm thick alumina substrate with dielectric constant of  $\epsilon_r = 9.9$ . First TiAu

was deposited on the backside of the wafer to form the large area ground plane. The circuit was patterned on the topside through a standard lift-off process using positive photoresist. For this purpose, a 300 nm thick DC magnetron sputtered niobium layer was deposited. Then a 150 nm thick palladium was deposited to define the contact areas of the circuit.

The measured performance of the fabricated bias-T is compared with the simulation results in Fig. 3.7a. One-port measurements were performed in LHe with the active device (SIS mixer) replaced by a 12.5  $\Omega$  resistor. This is done in order to evaluate the return loss across the band of interest. As predicted by circuit simulations, the measured return loss was better than -10 dB within the IF band. The circuit was integrated with a 385-500 GHz SIS DSB mixer [54], as shown in Fig. 3.7c. The measured noise temperature at 390 GHz was below 100 K over the entire IF band as shown in Fig. 3.7b. In comparison to the normal conductor-based bias-T [48, 49] a noticeable improvement in the flatness of the noise performance has been observed.

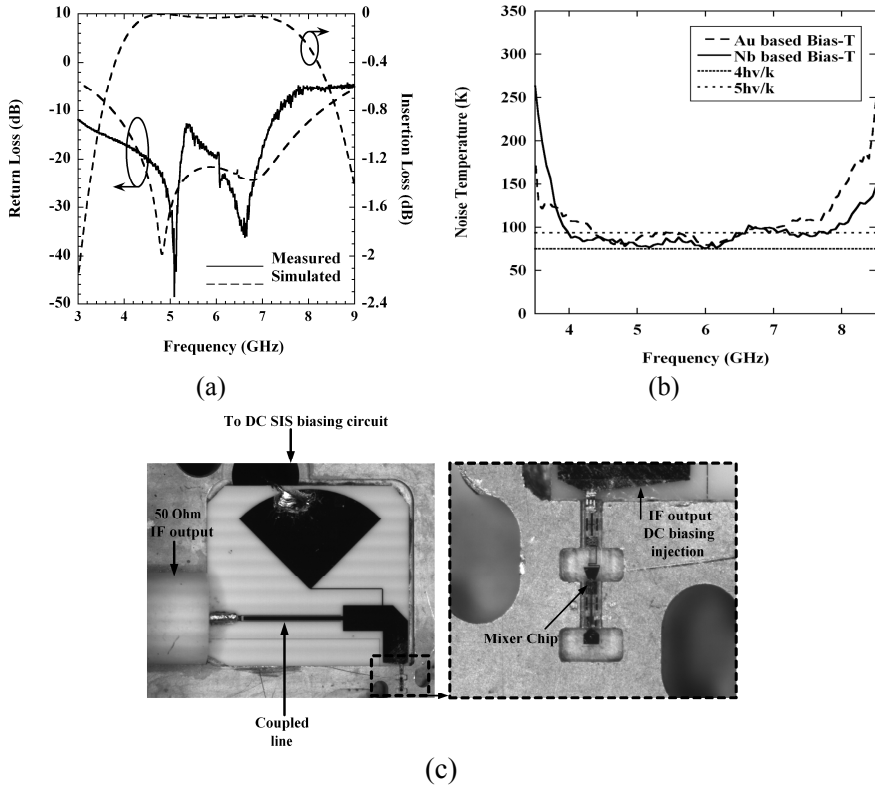


**Figure 3.7:** (a) Simulated and measured IF performance of the IF biasing circuit. (b) Noise temperature measurements of the SIS DSB mixer with Nb-based and Au-based bias-T across the IF band at 390 GHz. (c) Integrated SIS mixer chip with the bias-T circuit ( $9.0 \times 8.0 \text{ mm}^2$ ) with a close view of the SIS mixer chip placed into the channel.

### 3.2.3 Further Development

Due to excessive noise performance of the SIS mixer chip with on-chip LO injection circuitry at frequencies above 450 GHz, a revised mixer design was required. As a result, a new matching condition for the IF circuit was set, which required to modify the original design. Instead of an IF termination impedance of  $10\ \Omega$ , the output of the new SIS mixer had to be terminated to  $20\ \Omega$ . In comparison with the original arrangement shown in Fig. 3.7c, in the new design an additional single layer capacitor (SLC) was introduced. The capacitor resides outside the IF matching circuitry and is used as intermediate “landing point” for the bonding wire connecting the SIS chip and the IF circuitry, as shown in Fig. 3.8a and Fig. 3.8b. This type of topology acts as an L-C-L filter and offers a flatter IF response. A similar solution has been previously utilized in the ALMA Band 5 SIS mixer design [55]. The value of the SLC and the length of the bond wires were evaluated using a commercial circuit simulator [52].

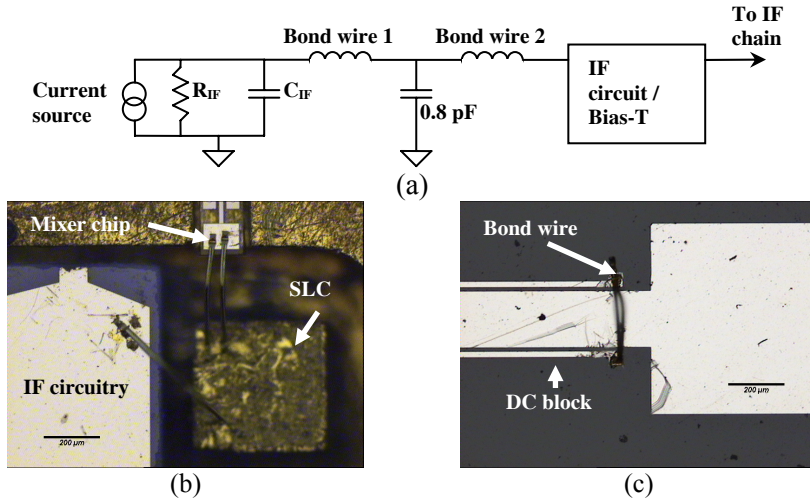


**Figure 3.8:** (a) IF equivalent circuit of the SIS mixer with the “landing” capacitor and IF biasing circuit used for the IF response simulations. (b) Modified design of the IF biasing circuit integrated with the SIS mixer chip and SLC. (c) A bond wire, linking the outer lines of the three-coupled microstrip line, was introduced in order to damp possible undesired resonances at higher IF frequencies.

The simulated complex IF impedance was optimized towards flat performance, as shown in Fig. 3.9a. The IF response at  $f_{LO} = 391\ \text{GHz}$  of the SIS receiver including the superconducting IF biasing circuit, installed at the APEX telescope, is shown in Fig. 3.9b. The measurement results confirmed significant improvement in the IF performance compared to the old results (see Fig. 7b). Now both ends of the IF band are considerably flatter.

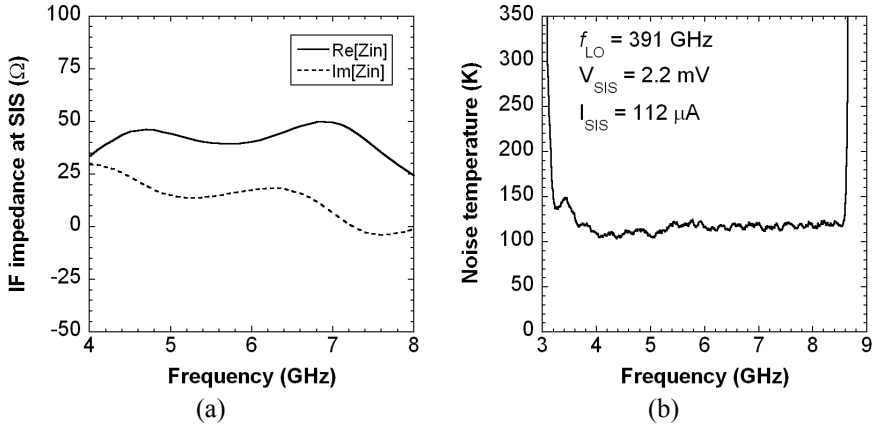


**Figure 3.9:** (a) Simulated IF load impedance of SIS mixer seen from the IF chain. At 6 GHz the IF load impedance is approximately  $40+i18$   $\Omega$ . (b) Receiver noise temperature across the IF band.

### 3.2.4 Summary

In this section, the development of an entirely planar superconducting biasing circuit for use in a SIS receiver has been demonstrated. The circuit was fabricated in-house and a good agreement between the simulated and measured performance has been achieved. The circuit was integrated in the 385-500 GHz SIS DSB mixer currently installed at the APEX telescope. This superconducting IF biasing circuitry can be further employed in 2SB receivers.

## Chapter 4

# Nb<sub>3</sub>Al High Energy-Gap Superconductor for Low-Noise THz Electronics

### 4.1 Overview and Motivation

Dominating technologies for high-resolution spectroscopy for mm and sub-mm wavelengths, used in all major radio astronomy instruments are the superconducting-insulator-superconductor (SIS) tunnel junction mixer and the hot electron bolometer mixer. The ability to provide low noise performance with noise temperatures close to the quantum limit makes the SIS mixer most attractive among other low noise technologies. The all-Nb (Nb/Al-AlO<sub>x</sub>/Nb) SIS technology is mature enough, so that it provides in a reproducible way SIS mixer chips

Broadening the frequency range of the SIS mixers has been pursued for long time since 80's by investigating high energy-gap superconductors such as NbN, NbTiN, and A15 materials (e.g., Nb<sub>3</sub>X (X = Al, Ga, Ge, Sn)). However, this development coincided with the time of the high- $T_c$  superconductors' discovery and that refocused a major part of the scientific interest, thus leaving the field underexplored.

This chapter is dedicated to extended studies of Nb<sub>3</sub>Al high-gap superconducting material, with a focus on thin film growth and characterization for further use in superconductor electronics applications, such as SIS tunnel junction and potentially a hot electron bolometer (HEB) [56]. With a reported bulk critical temperature of 18.9 K, low specific resistance value of 57  $\mu\Omega\text{cm}$  and demonstrated potential for thin film deposition [57], Nb<sub>3</sub>Al is a promising material for THz frequency low-noise applications. A proper combination of superconducting and tunnel barrier materials should allow to develop a new Nb<sub>3</sub>Al SIS junction technology that would provide extending the SIS technology above 1.2 THz, thus meeting the growing demands of ground and space-based radio astronomy, aeronomy and environmental sciences.

## 4.2 Properties of Nb<sub>3</sub>Al

### 4.2.1 Crystal Structure and Phase Diagram

The intermetallic compound Nb<sub>3</sub>Al was discovered in 1958 by Wood *et al.* [58] and a year later Corenzwit [59] reported that it is superconducting by measuring critical temperatures up to 18 K, depending on the composition. The Nb<sub>3</sub>Al structure consists of a cubic lattice with lattice parameter  $a = 5.18 \text{ \AA}$ . The 8-atoms basis is known as  $\beta$ -W or Cr<sub>3</sub>Si as part of the Pm3n space group. In the case of A<sub>3</sub>B structure, which Nb<sub>3</sub>Al belongs to, the B-atoms are arranged on a body-centered cubic (bcc) lattice and can be either transition or non-transition metals, whereas the A-atoms (Cr, Hf, Mo, Nb, Ta, Ti, V, W, Zr) are always transition metals and are ordered in face-centered cubic (fcc) lattice, as shown in Fig. 4.1.

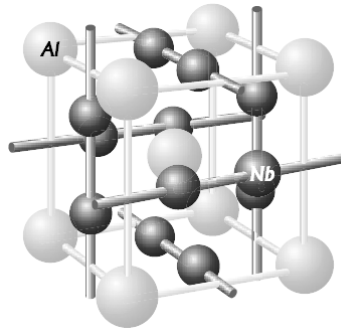


**Figure 4.1:** Distribution of Nb and Al atoms in A15 structure of A<sub>3</sub>B-type intermetallic compound Nb<sub>3</sub>Al demonstrating three orthogonal linear chains of Nb atoms. After A. Godeke [60].

According to the Nb-Al equilibrium phase diagram shown in Fig. 4.2a, there are three intermetallic phases, Nb<sub>3</sub>Al (A15 structure, Cr<sub>3</sub>Si type), Nb<sub>2</sub>Al (D8<sub>8</sub> structure,  $\sigma$ -CrFe type), NbAl<sub>3</sub> (D0<sub>22</sub> structure, TiAl<sub>3</sub> type) and one solid solution,  $\alpha$ -Nb. The three most referred phase diagrams are from Jorda [61], Svechnikov [62] and Lundin and Yamamoto [63], which vary on certain aspects as compositional ranges (due to Al loses by evaporation and measurement limitations at high temperature) and formation temperatures [64] but agreed on the fact that the stoichiometric Nb<sub>3</sub>Al is not in equilibrium at room temperature, i.e. it has a metastable nature. The Nb<sub>3</sub>Al phase is a peritectic phase and it occupies a region in the phase diagram that is adjacent to bcc and tetragonal phases. The value of  $T_c$  of Nb<sub>3</sub>Al is a function of the aluminium content and it reaches its highest point at compositions close to stoichiometric. It was found that superconducting critical temperature,  $T_c$ , is quite sensitive to the stoichiometric composition and degrades rapidly away from the stoichiometric point, as illustrated on Fig. 4.2b. According to Jorda *et al.* [61], the stoichiometric composition 25 at% Al (Nb<sub>3</sub>Al) with the lattice parameter  $a = 5.18 \text{ \AA}$  is metastable at room temperature and is only stable at 1940°C, or if prepared by quenching from that temperature. Therefore, not only stoichiometry but also the

fabricating technique is crucial for achieving high values of  $T_c$  for  $Nb_3Al$  material.

$Nb_3Al$  homogeneity area is adjacent to the areas of Nb-based solid solution and  $Nb_2Al$ , which both are superconductors with  $T_c$  up to 9.25 K and 13.5 K respectively. Thus, in case of additional phases, different than  $Nb_3Al$ , due to superconducting proximity effect, mixed up phases can be integrated without drastic degradation of the superconducting properties if the desirable phase dominates. In comparison, for the Nb-N system [65], adjacent to NbN-phase are the non-superconducting phases  $Nb_3N_4$  and  $NbN+N_2$ , and the resulting mixed-phases structure would exhibit extensive RF losses because of scattering and dissipating centers as confirmed by experimental measurements [66].

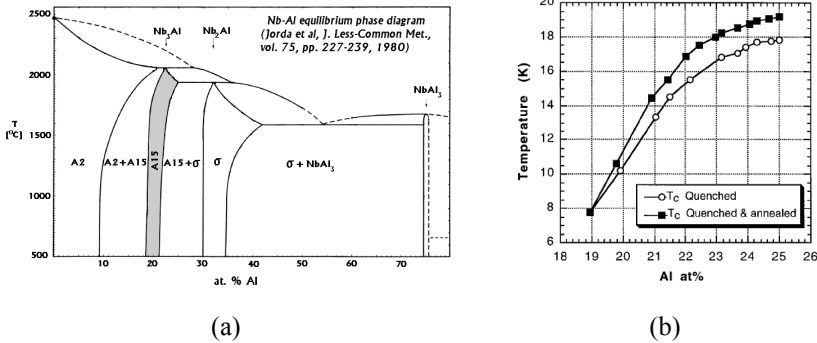


**Figure 4.2:** (a) Nb-Al equilibrium phase diagram. A2-phase refers to a solid solution of Al and  $\alpha$ -Nb bcc crystal lattice; A15 –  $Nb_3Al$  composition (shaded region);  $\sigma$ -phase – tetragonal  $Nb_2Al$  composition. (b) Changes of the critical temperature versus atomic composition of Al in A15 structure. After Jorda *et al.* [61].

## 4.2.2 $Nb_3Al$ as Superconductor

Intermetallic compounds with A15 crystallographic structure of the type  $Nb_3X$  ( $X=Al, Ga, Ge, Sn$ ) are known to be superconducting materials. Table 4.1 contains information about superconducting properties of several Nb-based superconducting materials, which are of an interest and used in mm- and sub-mm low-noise applications.

**Table 4.1:** Superconducting properties for several Nb-based materials [3].

Martial	$T_c$ (K)	$\lambda_L$ (nm)	$\xi_0$ (nm)	$H_{C2}$ (T)	$\Delta$ (meV)
Nb	9.25	39	52	0.08	1.45   $T_c=9.25$ K
NbN	16	200	5		2.56   $T_c=14$ K
NbTiN	17	~200	~4		2.50   $T_c=15$ K
$Nb_3Ge$	23.2	90	3	38	4.16   $T_c=23$ K
$Nb_3Sn$	18.5	90	4	24	3.39   $T_c=18.3$ K
$Nb_3Al$	18.9	90-200	4	29.5	3.04   $T_c=16.4$ K
$Nb_3(Al,Ge)$	21	130	1.5	44	-

Due to its very high  $H_{c2}$  and ability to carry extremely large electrical current densities with virtually no power losses, the  $\text{Nb}_3\text{Al}$  superconductor is a very attractive material for high magnetic fields applications. Certain applications such as particle beam handling magnets [67] and NMR magnets [68], operating in the 1 GHz frequency range.

### 4.2.3 $\text{Nb}_3\text{Al}$ Thin Films – Applications and Challenges

SIS mixer can be considered as an important high frequency application with biggest potential for  $\text{Nb}_3\text{Al}$  thin films. Providing high energy-gap,  $\text{Nb}_3\text{Al}$  material is capable of extending the operating frequency range of SIS mixer technology up to at least 1.5 THz. High quality  $\text{Pb}/\text{Nb}_3\text{X}$  ( $\text{X}=\text{Al}, \text{Ge}$ ) junction has been demonstrated by Tanabe *et al.* [57] as part of material diagnosis of the deposited films showing a sum gaps of 4.05 mV and 5.05 mV for  $\text{Pb}/\text{Nb}_3\text{Al}$  and  $\text{Pb}/\text{Nb}_3\text{Ge}$ , respectively. This gives a hope that  $\text{Nb}_3\text{Al}$  can also be similarly employed as a ground plane electrode in hybrid tunnel junctions, as referred above, or even in all- $\text{Nb}_3\text{Al}$  SIS junctions.

The quality of  $\text{Nb}_3\text{Al}$  films largely depend on the deposition conditions. Sufficient cause for degradation of the superconducting properties is attributed to an increased disorder and inhomogeneity in the films. Nonidealities in the material are due to presence of normal material could cause increased RF loss for applications such as tunnel junctions. Major challenge in the fabrication of all- $\text{Nb}_3\text{Al}$  SIS junction is to be able to maintain superior film properties together with high quality tunnel barrier that should withstand the high deposition temperature.

Due to the short coherence length,  $\xi_0 \sim 3\text{--}4$  nm, of  $\text{Nb}_3\text{Al}$  material, the use of “conventional” tunnel barrier, such as  $\text{AlO}_x$ , becomes problematic. The short coherence length and the high deposition temperature do not allow the use of “planarizing” Al layer, as in conventional  $\text{Nb}/\text{Al}/\text{AlO}_x/\text{Nb}$  tunnel junctions.

However, a possible way to realize an SIS junction based on  $\text{Nb}_3\text{Al}$  material is to utilize, for example, an AlN-barrier. Also, possible partial decomposition of the AlN barrier during the high-temperature deposition of the top  $\text{Nb}_3\text{Al}$ -based electrode is not going to induce severe degradation of the superconducting properties. This is because Al from the AlN barrier would produce only slight shift in the Nb-Al ratio, while nitrogen would likely form superconducting niobium nitride.

## 4.3 Fabrication and Characterization Techniques

This section describes the deposition and processing techniques used to obtain  $\text{Nb}_3\text{Al}$  thin films. First, a short overview of the early attempts to grow  $\text{Nb}_3\text{Al}$  layers is given. Then, an introduction to the currently used magnetron co-sputtering technique is presented. Next, a post-deposition rapid thermal annealing process is discussed as a way of enhancing the structural and superconducting properties of the co-sputter deposited  $\text{Nb}_3\text{Al}$  films. Finally, details concerning the employed instruments and measurements techniques are presented.

### 4.3.1 Overview of Existing Deposition Techniques for Nb<sub>3</sub>Al Thin Films

According to the phase diagram for the Nb-Al system [63], the stoichiometric A15 phase is stable only at high temperatures above 1800°C. However, the A15 phase is possible to be formed at relatively low temperature when the diffusion distance in Nb/Al diffusion system is reduced below 1 μm. Useful illustration for understanding the formation of the A15 superconductor is the mechanical alloying of initial Nb and Al powder mixtures [69]. The solid-state reactions can be described as follows:



One of the reasons for this type of reactions may be due to the fact that not enough energy is being supplied to Nb and Al in the elemental mixture to directly produce Nb<sub>3</sub>Al. Therefore, Nb<sub>2</sub>Al acts as a base for the Nb<sub>3</sub>Al formation through by adding Nb to its unit cell followed by subsequent heat treatment and conversion to Nb<sub>3</sub>Al. Therefore, in order to overcome the problem of low diffusion rate in Nb-Al system, the deposition is usually performed at considerably elevated temperatures or followed by subsequent annealing. Studies on Nb<sub>3</sub>Al films usually report substrate temperatures in the range 650-900°C, where diffusivity of Nb and Al is already enough to form complex A15 crystal structure.

In compound materials deposited by means of evaporation, it is difficult to attain uniform composition over the entire substrate area as well as uniform thickness. One possible technique to deposit alloys of the required composition uses a single source for evaporation. In this case, the composition of the alloy in the crucible should account for the selective evaporation of elements from the mixture. Thus, this makes the theoretical computation of the composition ration extremely difficult.

Another doable technique to deposit alloys through evaporation is the co-evaporation from several sources, one for each element, and condense the vapor on the substrate at the same time. The composition of the vapor streams is managed by the control of the evaporation rate of the individual sources. The ratio of the separation distance between, crucible and the distance sources-substrate gives the range over which adequate mixing of the vapors occurs, due to the directional nature of the vapor stream. Since the evaporation rate depends exponentially on temperature, a small variation in temperature of the source results in a large variation in the composition of the alloy film. Therefore, elements with widely varying vapor pressures, atomic masses as well as alloys with low concentration of solutes can be successfully deposited by the multiple crucible technique. The electron beam co-evaporation from two elemental sources, Nb and Al, has been demonstrated by Kwo *et al.* [70]. For 500 nm thick films the corresponding  $T_c$  was 16.5 K achieved with self-epitaxial growth of the film onto hot (950–1050°C) sapphire substrates. More often, deposition of Nb<sub>3</sub>Al

is reported utilizing magnetron sputtering, either DC [71, 72] or RF [73], from stoichiometric target.

It is common that where sputtering of A15 material from single target is employed, the levels of gas pressure are kept high up to 40 Pa due to thermalization reasons. In this case, the energy of the sputtered atoms is high on the order of several electron volts. For example, in sputtering Nb<sub>3</sub>Al from a composite target of Nb and Al, for an equal momentum transfer at the target the sputtered Al atoms would have approximately three times the energy of the sputtered Nb atoms due to roughly three times heavier mass for Nb. Therefore, by adjusting the gas pressure and target-to-substrate distance as well as accounting for the difference of the atomic masses, it is possible to maintain the required composition of the deposited alloy. As a direct measure of the thermalisation level (number of collisions, and hence energy loss) the pressure-distance product,  $PD$ , is usually used, where  $P$  is the sputtering gas pressure and  $D$  is the target-substrate distance. It was found by several groups that in order to achieve higher values of critical temperature at low pressures it is necessary to increase the target to substrate distance. This approach is equivalent to that produced by high pressure and short distance sputtering. Typical  $PD$ -values for A15 superconductors are shown in Table 4.2 based on previous investigations on A15 materials [72, 74, 75].

**Table 4.2:** Pressure-distance (PD) products for several A15 compounds deposited by magnetron sputtering from alloy targets.

Material	$T_c$ [K]	$PD$ [Pa mm]	Ref.
Nb <sub>3</sub> Sn	18.3	300–400	[75]
Nb <sub>3</sub> Ge	> 22	1000–2000	[74]
Nb <sub>3</sub> Al	> 17	1000–2000	[72]

As mentioned earlier in this chapter, the formation of A15 phase requires high enough substrate temperature in order to produce superconducting films with  $T_c$  closer to that of the bulk material. So far, it was discussed the possibilities of depositing A15 materials by using high substrate temperature (700-900°C), either by evaporation or sputtering. However, room temperature sputtering of Nb/Al multi-layers is another alternative to deposit Nb<sub>3</sub>Al. This technique involves further heat treatment in order to obtain the A15 phase. Several groups [76-78] have studied the phase formation sequence in sputter-deposited multilayer Nb<sub>3</sub>Al films. The highest  $T_c$  achieved by this approach was 16.2 K for 400 nm thick film on a sapphire substrate [78].

Deposition of thin films of materials with metastable intermetallic phases, such as A15, has also been reported with the help of pulsed laser deposition (PLD) technique [79] for Mo-Re films.

All described above deposition methods of Nb<sub>3</sub>Al and other A15-type materials suffer from a number of problems, such as costly alloy targets (in which the composition of elements must be adjusted upon determining resulting

composition of the deposited films), extremely high argon pressure needed and difficulties to produce ordered metastable phases.

### 4.3.2 Co-sputtering of Nb<sub>3</sub>Al and Dedicated Equipment

In attempt to address the above issues, in this work an alternative approach in depositing Nb<sub>3</sub>Al has been studied using a dedicated sputtering system, as shown in Fig.4.3a. The method is based on a DC magnetron co-sputtering from two confocally arranged 2" Nb and Al magnetron targets onto 4" heated rotating substrate holder, as illustrated schematically in Fig. 4.3b. Co-sputtering from con-focally arranged sputtering sources onto rotating substrate provides an opportunity to have tight and independent control over both stoichiometry and uniformity of the deposited films.

The sputtering system employed in this work is equipped 500 l/s turbomolecular pump, resulting in ultimate pressure of  $2 \times 10^{-8}$  Torr. Moreover, the system is equipped with a load-lock module in order to improve the vacuum conditions, reduce the residual water as well as to shorten the turn-around time by avoiding long pumping time.

Hot substrate is a useful option for activating diffusion ordering of Nb<sub>3</sub>Al film structure for the time of the deposition. The maximum available substrate temperature was 850°C, and after deposition, the substrate was left to cool down to below 200°C in less than 20 min.

In terms of stoichiometry, the film composition was maintained through calibrated deposition rates ratio for each material as function of the DC bias of the magnetron sources. In this work, Al content in the films was varied within the range 12-26 at. % Al.



**Figure 4.3:** (a) Dedicated equipment for growth of Nb<sub>3</sub>Al superconducting films and SIS tunnel junction fabrication [80]; (b) schematic view of confocal arrangement of the elemental targets for DC magnetron co-sputtering deposition onto rotating sample holder.

### 4.3.3 Heat Treatment and Post Annealing of Nb<sub>3</sub>Al Films

From its inception, the DC magnetron co-sputtering method was thought to provide stoichiometric Nb<sub>3</sub>Al thin films. However, the superconducting transition temperature,  $T_c$ , of co-sputtered samples was found to be somewhat lower than that of the best reported A15 films. In order to anneal the structural defects,

created during the deposition, and improving the superconducting properties, an additional rapid heating treatment has been applied in order to facilitate bcc to A15 transformation. The transformation typically [64] occurs at fast heating rates as soon as the temperature reaches 900-1000°C. Fast heating leads to bypass the B2-ordering of the bcc phase, ordering which is thought to lead to the formation of the Al rich planar faults [81]. Furthermore, the short heating time does not permit significant grain growth [82].

Typical heat treatment was carried out in argon atmosphere for 30 s, going to 1000°C for 20 s as starting from 550°C in order to avoid temperature overshooting at the setpoint. Subsequently, the annealing process was followed by fast cooling in argon atmosphere. As a result of the applied fast annealing process, a significant improvement in the superconducting properties was achieved. This is discussed in more details further in *Section 4.4*.

### 4.3.4 Characterization Techniques

In this work, the crystal structure and lattice properties of the material were characterized by X-ray Diffraction (XRD) using Phillips X'Pert Diffractometer. It is equipped with a copper anode tube with radiated wavelength  $\lambda_{Cu}^{K\alpha} = 1.5405980 \text{ \AA}$  operating at 40 mA and 40 kV. Most of the scans ( $2\theta$ - $\omega$  and  $\omega$ -scans) were made with a rocking-curve setup having a point focus and primary optics consisting either of a Ge(220) 4-crystal monochromator with crossed slits or a cross-slit collimator with a Ni filter. Secondary (diffracted beam) optics consist of rocking curve attachment with a proportional detector and a divergence slit between  $1/2^\circ$  and  $1/16^\circ$ . For two-dimensional mapping ( $2\theta$ - $\omega$ - $\omega$  scans), a triple axis attachment was used as a secondary optics module thus providing high resolution diffraction space maps.

Grain size and roughness analysis of the deposited films were estimated with the help of Atomic Force Microscopy (AFM). The AFM topography images were obtained with a Nanoscope Dimension 3000 SPM from Digital Instruments [83] operating in a tapping mode (the tip-sample interaction was kept constant through steady oscillation amplitude). The images were obtained over an area of  $1 \times 1 \mu\text{m}^2$ , with a scanning rate of 2 Hz as Pt coated Si cantilever was used for all AFM studies.

Identification of film compositional profile was performed in collaboration with Moscow Power Engineering Institute by using a technique called Spectroscopy of Reflected Electrons (SRE) [84, 85]. This method is capable of analyzing higher range of electron energy losses ( $\geq 300 \text{ eV}$ ), thus reaching much deeper layers compared to traditional implementation of reflected electron energy loss spectroscopy (REELS).

The cross-section imaging and thickness characterization of the  $\text{Nb}_3\text{Al}$  films were done by High-Resolution Transmission Electron Microscopy (HRTEM). Cross-sectional specimens were prepared in FEI Strata235 DualBeam work station, which accommodates ion milling, imaging and material deposition by means of focused ion beam (FIB). A Phillips CM200 transmission electron

microscope was used for high-resolution imaging provided by collaboration with the Nanofabrication Laboratory at Chalmers University of Technology.

Superconducting transition temperature was measured utilizing a four-probe technique and performed either in a He-dewar using a dipstick or in a close-cycle 12 K cryo-cooler. The temperature was recorded with accuracy of  $\pm 0.1$  K through a calibrated Si-diode temperature sensor [86]. A dedicated sample adapter unit was designed and implemented for characterization of small samples with an area of  $5 \times 5$  mm<sup>2</sup>, thus avoiding any wire bonding, as shown in Fig. 4.4. The unit consists of stacked Fiberglass printed circuit boards with installed four Alpha Test spring-loaded probes maintaining the electrical contact through the PCBs between the wafer and the dipstick wiring circuitry.

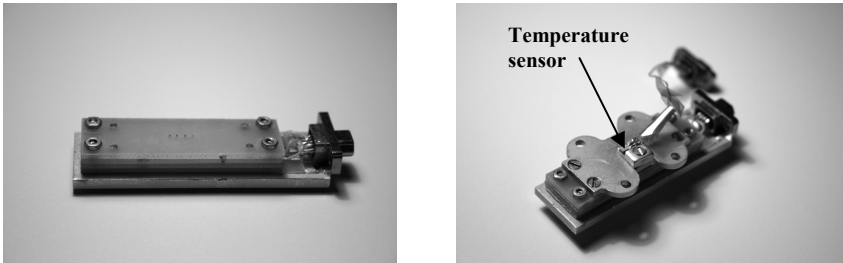


**Figure 4.4:** Photos of the sample adapter unit used in resistance-temperature measurements of Nb<sub>3</sub>Al films.

Critical field measurements were performed in Oxford MagLab System 2000 equipped with a 5 T (at 2.2 K) Nb-Ti superconducting magnet and a variable temperature insert (VTI). Hence, the operational temperature range is 2–400 K. A standard four-probe technique was employed with a magnetic field applied parallel to the film surface. The selected samples were measured using the facilities of the Quantum Device Physics Laboratory at Chalmers University of Technology.

## 4.4 Results and Discussion

### 4.4.1 Heteroepitaxy on Nb Seed Layers

Study on the films' stoichiometry in terms of compositional depth profile was conducted by SRE method. Figure 4.5 illustrates the film stoichiometry vs. the film thickness of as-deposited Nb<sub>3</sub>Al films on oxidized silicon substrates for two different nominal concentrations, namely 12 at.% Al and 24 at.% Al, showing a strong Al depletion from the film surface side, while at the substrate side, aluminum segregation was observed.

The result of the SRE analysis clearly pointed out that the choice of an appropriate substrate is of a great importance for obtaining good quality films. That had led us to the suggestion that a substrate or a buffer layer with properties close to the Nb<sub>3</sub>Al crystal structure should provide enhanced growth conditions as

well as prevent diffusion of foreign elements such as O<sub>2</sub> and Si. Following that, it was then tried Nb underlayer and YSZ substrate as discussed later.

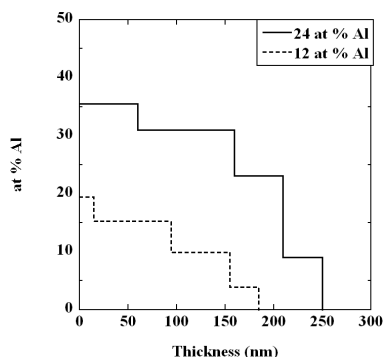


**Figure 4.5:** Dept profiles of Nb<sub>3</sub>Al thin film deposited on AlN/SiO<sub>2</sub>/Si substrate. The Al content of the film is 12 at.% (dashed) and 24 at.% (solid), respectively.

The major progress in this work was achieved in Nb<sub>3</sub>Al films grown on thin niobium seed layer. In order to improve the nucleation conditions for Nb<sub>3</sub>Al at the substrate surface, a thin Nb layer was deposited prior deposition of the Nb<sub>3</sub>Al. The Nb underlayer was DC magnetron sputtered at 10 Å/s deposition rate having a well ordered and textured (110) columnar structure, which was verified by XRD analysis. In other words, the Nb<sub>3</sub>Al film phase grows along the <210> direction in conjunction with the <110> direction of the Nb seed layer. Derivation of the crystallographic relationship between Nb<sub>3</sub>Al and Nb is presented in *Appendix A*. Other studies have reported Nb(100) || Nb<sub>3</sub>Al(211) to be the favored orientation relationship [87] but this was not observed in the current studies. A TEM image and XRD scan of the Nb<sub>3</sub>Al films grown on Nb seed layer are presented in Fig. 4.6.

The initial nucleation conditions created by the Nb underlayer had resulted in deposited Nb<sub>3</sub>Al film with enhanced structural ordering, compared to films without such Nb seed layer. However, in terms of superconducting properties, e.g. critical temperature and resistivity residue ratio (RRR), the as-deposited Nb<sub>3</sub>Al films exhibit at most  $T_c$  of 12 K and RRR of 1.1. It was assumed that the disorder in the film is responsible for the suppressed superconducting properties. Improvement in the film quality was seen in *ex-situ* rapid thermal annealing (RTA) of the as-deposited films. A rapid heating up to 1000°C in argon atmosphere for 30 s has been applied followed by free cooling in argon. This resulted in even further ordering of the A15 phase, and increased  $T_c$  up to nearly 16 K. However, the high temperature annealing should be made fast enough in order to avoid intense growth of Nb<sub>2</sub>Al which may lead to suppression of the superconductivity and increased values of the specific resistance.

The RTA treatment resulted in more ordered Nb<sub>3</sub>Al films and having a higher  $T_c$ . Best parameters were achieved for film with 24 at.% Al, namely a  $T_c$  of 15.7 K with transition width,  $\Delta T_c = 0.2$  K and RRR~1.6. The dependence of critical temperature on Al concentration is graphically shown in Fig. 4.7 and

compared to as-deposited films. The latter ones exhibited at most a  $T_c$  of 12 K, for 16 at.% Al films. These results suggested that the growing film suffers from low diffusion mobility of Nb and Al atoms during deposition. It is also worth mentioning that the targeted thickness of the film, suitable for SIS tunnel junction application, is in order of 300 nm at most. For the thinner films presented here, this clarifies the differences in  $T_c$  from other published results on Nb<sub>3</sub>Al.

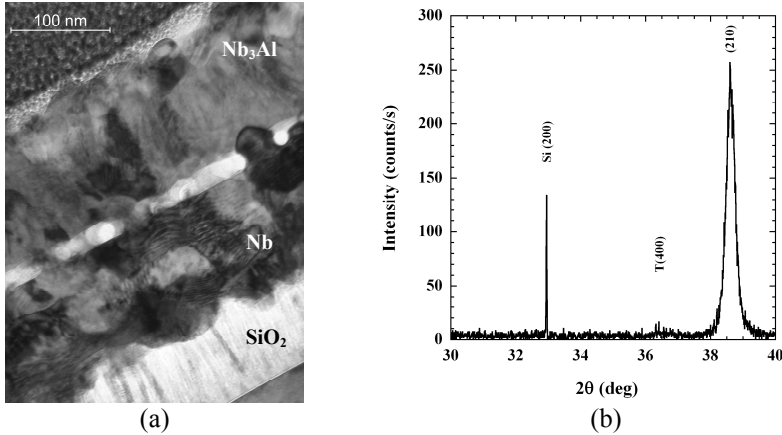


**Figure 4.6:** (a) Cross-sectional TEM image of Nb<sub>3</sub>Al grown on Nb/SiO<sub>2</sub>/Si substrate. (b) X-ray diffraction pattern of Nb<sub>3</sub>Al film grown on Nb underlayer. The Nb<sub>3</sub>Al(210) peak coincides with the Nb(110) one therefore the broadening.

The depth dependence of the Nb and Al composition for as-deposited and annealed Nb<sub>3</sub>Al films has been studied. For this purpose, the film was thinned with a help of ion beam etching and measured  $T_c$  of the partially etched films. Measurements of the critical temperature at different film depths are illustrated in Fig. 4.8, demonstrating that etching away of the first ~130 nm thick layer (counting from the Nb<sub>3</sub>Al film surface) does not affect the measured film  $T_c$ , thus suggesting that the film at the surface possess uniform ordered A15 structure. Apparently, deeper in the film, the value of the critical temperature deteriorates substantially. This might be attributed to the film quality at the Nb/Nb<sub>3</sub>Al interface as well as the reduced thickness.

Further studies on the structural properties were done by examination of the grain size by XRD, AFM and TEM techniques. Estimation of the mean grain size of the film is of high interest because it gives useful information about deposition, crystallization and possibly phase transition phenomena in the film. Also, information about the grain is valuable from the prospective of microwave applications, as “weak links” have significant impact on the surface impedance, e.g. the RF residual losses. In this study, a scanning probe imaging processor (SPIP) software was used for estimation of the mean grains’ diameter and perimeter from the AFM images of as-deposited and annealed Nb<sub>3</sub>Al specimens, as shown in Figure 4.9. The average diameter size of the former one appeared to have a double peak at 30 nm and 50 nm, i.e. containing simultaneously smaller and larger grains. After annealing, the majority of grains acquire nearly the same

grain size of about 50–60 nm, thus suggesting for a re-crystallization process resulting in sufficiently lower concentration of crystal defects.

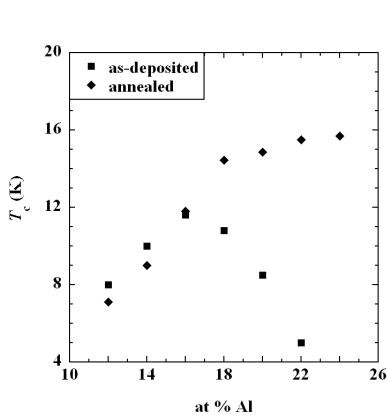


**Figure 4.7:** Superconducting transition temperature vs. alloy composition for as-deposited (■) and annealed (◆) samples.

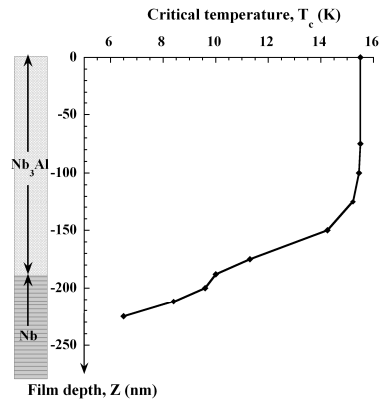


**Figure 4.8:** Critical temperature depth profile of an annealed Nb<sub>3</sub>Al film. The Nb<sub>3</sub>Al film was deposited on Nb seed layer and had a thickness of ~130 nm. The film was thinned by argon ion milling and subsequently  $T_c$  was measured after each etching step.

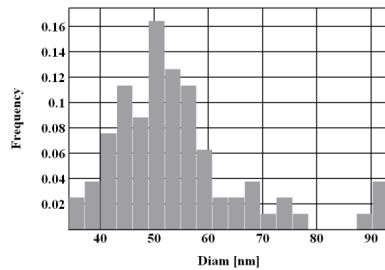
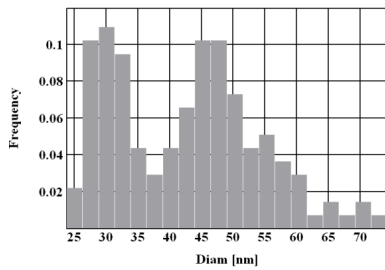
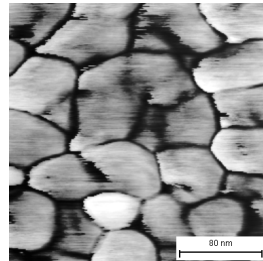
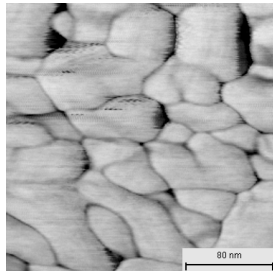


**Figure 4.9:** AFM images and histograms of the grain diameter of (a) as-deposited and (b) post-annealed Nb<sub>3</sub>Al film at 1000°C.

## 4.4.2 Estimation of Superconducting Parameters

Best Nb<sub>3</sub>Al films with 24 at.% Al have been subsequently studied to estimate the most important superconducting parameters such as the penetration depth, the upper critical field, the coherence length, and the diffusion coefficient, following the methodology described in [88].

The penetration depth was estimated using the Ginzburg-Landau (GL) expression in the weak-coupled BCS in dirty limit:

$$\lambda_{GL}^{BCS}(0) = 6.42 \times 10^{-6} \left[ \frac{\rho(\mu\Omega \text{ cm})}{T_c} \right]^{1/2} \quad (4.2)$$

Critical current ( $I_c$ ) measurements were conducted on patterned Nb<sub>3</sub>Al thin films. The basic test structure was Nb<sub>3</sub>Al microbridge with widths  $W = 5\text{--}20 \mu\text{m}$ , and fixed length,  $L = 70 \mu\text{m}$ . The bridge structures were defined by photolithographically and subsequent reactive ion etching (RIE). The Nb<sub>3</sub>Al film had a thickness  $d = 150 \text{ nm}$ . Critical current measurements were limited to a maximum of 20 mA by the biasing circuit.

Critical current density commonly observed in bridges made of A15 materials has a power law dependence,  $J_c \sim (1 - t)^n$ , where  $t = T/T_c$  is the reduced temperature [89]. For inhomogeneous type-II superconductors, a temperature variation of [90]:

$$J_c(T) = J_{c0}(1 - t)^{5/2} \quad (4.3)$$

where  $J_{c0} = 4.3 \times 10^7 \text{ A/cm}^2$  is the critical current density at 0 K extracted from the fit. Near  $T_c$ , the measured  $J_c(T)$  curves, shown in Fig. 4.10, fit eq.(4.3). This temperature dependence on bridges with different cross section areas on the same sample has been experimentally verified.

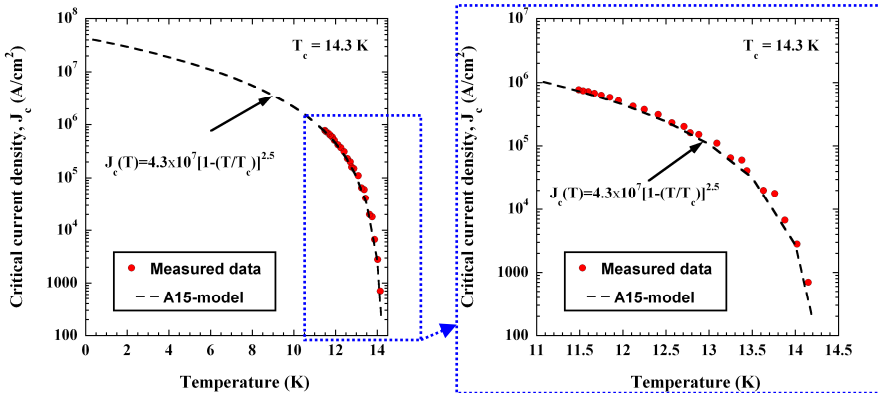


**Figure 4.10:** Temperature dependence of the critical current density of Nb<sub>3</sub>Al film deposited on a Nb/SiO<sub>2</sub>/Si. The bridge dimension is  $0.2 \times 5 \times 70 \mu\text{m}^3$ . Dashed lines represent the fit from eq. (4.3).

The approximated high current density,  $j_c > 10^7$  A/cm<sup>2</sup> at  $T = 4.2$  K, obtained from the bridges indicated a homogeneous film structure free from sufficient weak links.

Measurements of critical-field slopes near  $T_c$ ,  $(dH_{c2}/dT)_{T_c}$ , combined with the Ginzburg-Landau-Abrikosov-Gor'kov (GLAG) relationships for type-II superconductivity provide a set of superconducting material parameters, e.g.  $\xi_{GL}(0)$ ,  $\xi_0(0)$ ,  $D$  and  $l$  for Nb<sub>3</sub>Al material. The zero-temperature GL coherence length,  $\xi_{GL}(0)$ , is calculated from the measured  $(dH_{c2}/dT)_{T_c}$ -slope, Fig. 4.11, using the relationship:

$$-\left. \frac{dH_{c2}}{dT} \right|_{T_c} = \frac{\hbar c}{2e} \frac{1}{\xi_{GL}^2(0)} \frac{1}{T_c} \quad (4.4)$$

where  $\hbar$  is the Planck's constant,  $c$  is the velocity of light, and  $e$  is the electron charge.

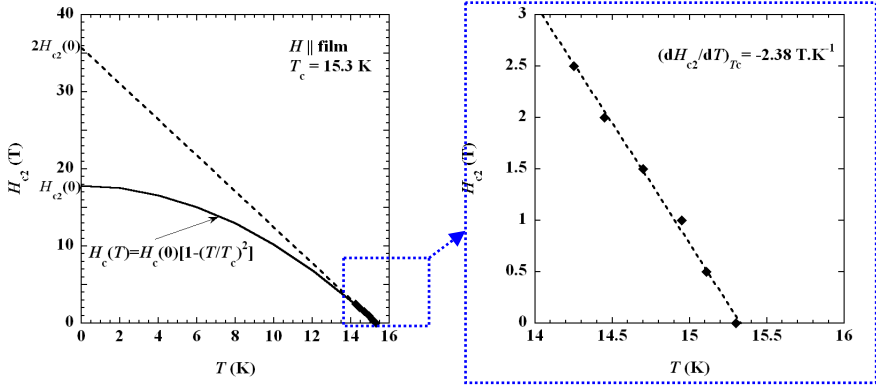


**Figure 4.11:** Temperature dependence of the critical fields near  $T_c$  for Nb<sub>3</sub>Al film with 22 at.% Al. The applied magnetic field was parallel to the sample surface.

Also, the BCS coherence length,  $\xi_0$ , was estimated from the zero-temperature critical field value,  $H_{c2}(0)$ , by:

$$\xi_0(0) = \left[ \frac{\Phi_0}{2\pi H_{c2}(0)} \right]^{1/2} \quad (4.5)$$

where  $\Phi_0 = h/2e$  is the magnetic flux quantum.

The diffusion coefficient [91] of the electrons at the upper critical field,  $D$ , was also calculated from the  $(dH_{c2}/dT)_{T_c}$ -slope by employing eq.(4.6).

$$D \approx 10^4 \left[ \left( -\frac{dH_{c2}}{dT} \right)_{T_c} \right]^{-1} \quad (4.6)$$

Then, the electron mean free path,  $l$ , can be calculated by:

$$D = \frac{v_F l}{3} \quad (4.7)$$

where the value for the Fermi velocity,  $v_F = 2 \times 10^7 \text{ cm s}^{-1}$  [92].

The measured and estimated values of the superconducting and normal-state properties derived from the Nb<sub>3</sub>Al film characterization are shown in Table 4.3. The results are in agreement with the published data on Nb<sub>3</sub>Al. For these calculations, it has been assumed that there is no paramagnetic limiting [88].

**Table 4.3: Some important superconducting and normal-state material properties of 300<sup>o</sup> nm thick Nb<sub>3</sub>Al.**

$\rho_{20K}$ ( $\mu\Omega \text{ cm}$ )	$T_c$ (K)	$\xi_0$ (nm)	$\xi_{GL}(0)$ (nm)	$D$ ( $\text{cm}^2 \text{ s}^{-1}$ )	$l$ (nm)	$\lambda_{GL}(0)$ (nm)
163	15.3	4.3	2.8	0.4	0.6	210

These properties are expected for “dirty” thin films, taking into account the high value of the specific resistance as well as the difference between  $\xi_0$  and  $\xi_{GL}$ . In comparison with other superconducting materials used in mm- and submm thin film technology, such as Nb, NbN and NbTiN, the results on Nb<sub>3</sub>Al presented here show a close correlation. In terms of diffusion constant, these three materials exhibit typically values of  $1.6 \text{ cm}^2 \text{ s}^{-1}$  [63],  $0.4 \text{ cm}^2 \text{ s}^{-1}$  [93] and  $1.13 \text{ cm}^2 \text{ s}^{-1}$  [94], respectively, which suggests that Nb<sub>3</sub>Al material could be a possible candidate for fabrication of hot electron bolometer devices.

#### 4.4.3 Epitaxial Growth of Nb<sub>3</sub>Al Thin Films on YSZ

During the 1970’s and 80’s the interest in the A15 materials was significant, thus resulting in quite extensive research including also the possibility to grow films epitaxially. This was done in order to obtain better film properties, which comparable to the bulk material. The epitaxy greatly improves the film crystallinity in the initial deposition layer, thereby improving the superconducting properties. A number of substrates and buffer layers have been tried out for the growth of A15 materials including self-epitaxy [95] and seed layers of Nb<sub>3</sub>Ir and Nb<sub>3</sub>Rh [96, 97].

Biggest potential has been seen in yttria-stabilized zirconia (YSZ), which was demonstrated by Asano *et al.* [98] to grow Nb<sub>3</sub>Ge. YSZ has a cubic structure with lattice parameter ranging between 0.507 nm and 0.520 nm depending on the Y<sub>2</sub>O<sub>3</sub> content [99, 100]. Thus, the theoretical lattice mismatch between the YSZ substrate and bulk Nb<sub>3</sub>Al can easily be less than 1% which offers a good opportunity to grow epitaxial high quality Nb<sub>3</sub>Al films and even to explore a new

range of device applications for Nb<sub>3</sub>Al, such as the hot electron bolometers (HEBs).

In this study 9.5%mol Y<sub>2</sub>O<sub>3</sub>, (100)-orientation, and 5×5×0.5 mm<sup>3</sup> YSZ substrates were used [101]. The lattice constant was  $a = 5.13 \text{ \AA}$  and having a surface roughness of 0.8 nm. Hence, the corresponding lattice mismatch between the YSZ substrate and Nb<sub>3</sub>Al material ( $a = 5.18 \text{ \AA}$ ) is about 1%.

A structural characterization of the magnetron co-sputtered Nb<sub>3</sub>Al thin films was performed by TEM. Figure 4.12 shows a cross-sectional TEM micrograph taken from a Nb<sub>3</sub>Al film grown on YSZ(100) substrate. One can see that in the first few nanometers the Nb<sub>3</sub>Al film exhibits the same lattice structure as the underlying YSZ, suggesting that the film grown was epitaxial.

Crystal structure and film quality of the deposited Nb<sub>3</sub>Al film was studied by means of X-ray diffraction. The lattice constant of the Nb<sub>3</sub>Al film was found to coincide with the one of YSZ, i.e.  $a = 5.130 \text{ \AA}$ . This demonstrates that the Nb<sub>3</sub>Al film has the same lattice plane spacing as the underlying YSZ substrate the film and is preferentially (100)-oriented as a result from the epitaxial relationship between the Nb<sub>3</sub>Al film and YSZ substrate.

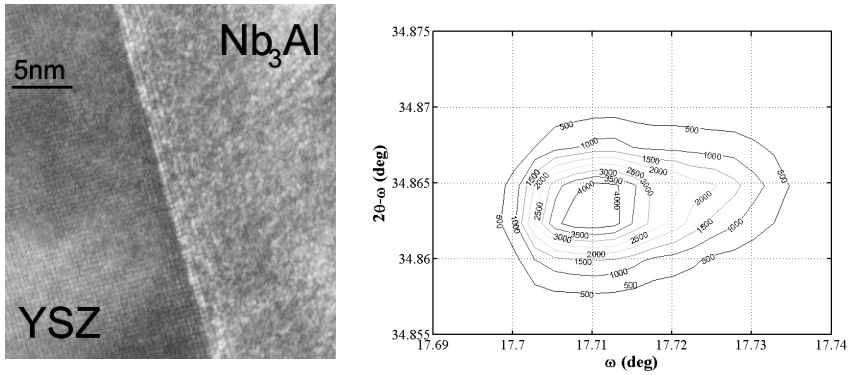


**Figure 4.12:** (To the left) A Cross-sectional TEM micrograph of a 230 nm thick Nb<sub>3</sub>Al film grown on YSZ substrate. (To the right) An XRD 2D map of Nb<sub>3</sub>Al film with 16 at.% Al grown on YSZ(100).

The Nb<sub>3</sub>Al films deposited on YSZ is likely to be strained to the substrate. So far, it has not been possible to obtain perfectly, or even partially, relaxed Nb<sub>3</sub>Al films on YSZ. An example of the peak shape from a 2D  $2\theta-\omega-\omega$  map is shown in Fig. 4.12. The reflection corresponds to YSZ(200) and its prolongation is due to the Nb<sub>3</sub>Al(200). The scan confirms the lack of relaxation along the  $2\theta$  axis as well as the present disorder by the broadened  $\omega$ -peak. As a direct measure for the disorder, the RRR and the transition width can be considered, representing the scattering on the structure defects. Fig. 4.13 shows an R-T measurement of deposited Nb<sub>3</sub>Al, which exhibits the highest  $T_c$  for those films on YSZ. Typical values for RRR vary close to 1.1 while  $\Delta T_c$  is within 1-2 K. Moreover, along with broad transition it also resulted in suppressed critical temperature down to 12.3 K. These estimates of  $T_c$  and RRR, however, remind to those obtained from as-deposited Nb<sub>3</sub>Al films on Nb underlayer.

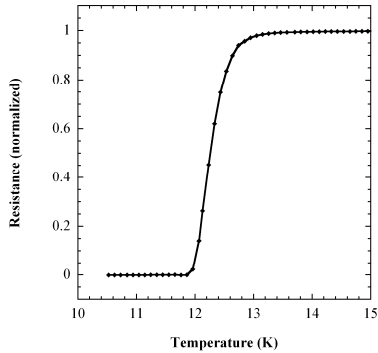


**Figure 4.13:** Highest  $T_c$  observed in a 230 nm thick  $Nb_3Al$  as-deposited film with 16 at.% Al grown on YSZ substrate.

Although the  $Nb_3Al$  film exhibited monocrystalline structure in the first few monolayers at the  $Nb_3Al/YSZ$  interface, apparently there is significant disorder as film grows thicker. This can be attributed to the relatively high deposition rate used or due to excessive energy of the arriving Nb and Al atoms. Moreover, because of slight lattice mismatch, epitaxial  $Nb_3Al$  thin films possess internal strain, which may lead to crystal structure modification or create defects and thus change some properties of the material.

Similarly to the approach with films grown on Nb seed layer, thermal annealing of those films could result in more strain-relaxed  $Nb_3Al$  films. So far it has not been possible to achieve substantial improvement of the superconducting properties by rapid thermal heating. However, due to accumulation of extra energy, strained epitaxial  $Nb_3Al$  film must release its excess energy one way or another when the film gets thicker. The transformation from stressed film to relaxed film can be spontaneous or through extraneous means, such as post-deposition heat treatment. Spontaneous strain releasing often results in many kinds of defects (dislocations) and therefore the intention is to focus more on the optimization of the deposition parameters.

To summarize, the outcome of the provided study demonstrates the possibility of growing monocrystalline  $Nb_3Al$  film by epitaxy on yttria stabilized zirconia substrates, which was confirmed by both XRD and TEM techniques. These initial results suggest further optimization of the deposition parameters, hence revealing a large margin for improvement of the film quality. Regardless the film structure, for THz applications the dielectric properties of the substrate are of crucial importance. The dielectric constant of YSZ is about 27 with a loss tangent  $5.4 \times 10^{-3}$  at 1 MHz [102] which limits the usage of YSZ substrate for high frequency applications due to substantial dielectric losses. However, the technology for heteroepitaxial growth of thin buffer layers of YSZ on substrates with low-loss and lower dielectric constant, such as Si [103], will allow wider range of applicability within the low-noise THz electronics.

## 4.5 Summary

This *Chapter* summarized the extensive work on the deposition and characterization of superconducting Nb<sub>3</sub>Al thin films for use in low-noise THz application such as SIS and HEB mixers. The films have been realized for the first time by means of DC magnetron co-sputtering from two elemental targets. Best films were obtained through heteroepitaxy on Nb underlayer, followed by subsequent rapid thermal annealing. Post annealing by rapid thermal heating was found to be a key process step in achieving ordered and higher quality Nb<sub>3</sub>Al films with  $T_c$  as high as 15.7 K and critical current density of  $\sim 2 \times 10^7$  A/cm<sup>2</sup> at 4.2 K. The crystal structure of the films was investigated by using XRD and TEM observations. Single-crystal YSZ substrates have been found to promote the epitaxial growth of the Nb<sub>3</sub>Al thin films. This result might be of importance for applications such as the hot-electron bolometer.

## Chapter 5

### Towards Integrated THz Array Receivers

Heterodyne instrumentation for THz ground - based telescopes, airborne and space observatories have made remarkable progress during the last two decades bringing SIS and HEB mixer technology to its ultimate state [26, 104, 105]. However, very few installed receivers really break terahertz frequency threshold so far. In particular, the dominating technology above 1 THz employs quasioptical HEB mixer design with planar antenna and substrate lens [106, 107]. Alternatively, waveguide HEB mixers have been also demonstrated [26, 108, 109] offering superior efficiency of the receiver-antenna coupling via a corrugated horn.

In this *Chapter* a design of a waveguide balanced HEB mixer, covering the frequency band 1.6-2.0 THz, is considered. A novel layout employing membrane-beam and surrounding supporting substrate for mixer assembly and electrical interfacing is presented. Moreover, a special attention is paid to the physical properties of ultra-thin NbN film as they are essential for the HEB's operation. An important achievement of this work is also the fabrication of HEB devices based on epitaxial ultra-thin NbN film deposited on 3C-SiC/Si substrate.

#### 5.1 Design of a Balanced Waveguide HEB Mixer

##### 5.1.1 Mixer Layout

Generally, the waveguide type of design is considered to be beneficial for instrumentation [9] and specially for HEB mixers: primarily, it allows to use the most effective feed, namely, the corrugated horn. Moreover, HEB waveguide based mixers have reduced direct detection response due to natural limitation of the RF band. In addition, the balanced configuration allows for effective use of the available local oscillator (LO) power [26].

In contrast to the mixer presented in [26], the proposed design employs split-block technique for the whole mixer block. The mixer layout is schematically shown in Fig. 5.1 and consists of input waveguides connecting to the RF and LO corrugated horn, a waveguide 3-dB 90° hybrid and mixer chip mounts. This arrangement provides reduced lengths of the RF signal waveguide, respectively lower RF losses, by placing the 3-dB 90° hybrid as close as possible to the horn antenna. In addition, a novel layout for the mixer chip is used: the mixer chip has a half-frame of thick silicon supporting a very thin beam, where an HEB mixer

with its circuitry. The beam is placed across the waveguide. IF/DC bias-T is integrated onto the frame part of the mixer chip.

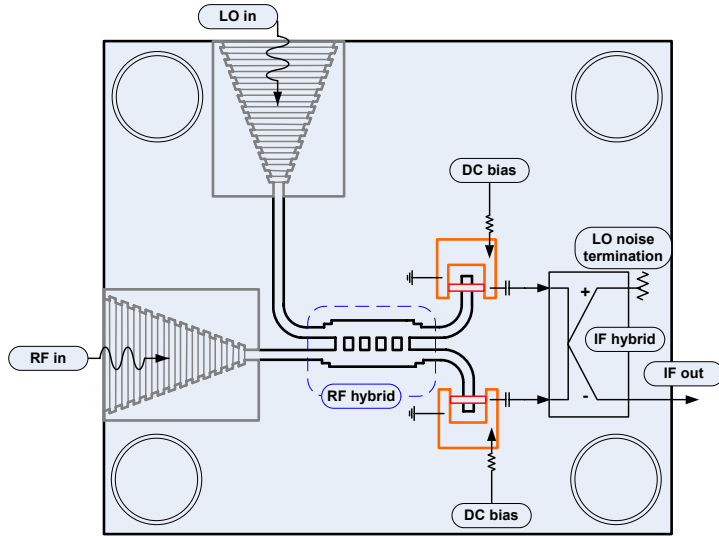


**Figure 5.1:** Proposed mixer layout. The balanced waveguide mixer consists of corrugated horns (for RF and LO) connected to a waveguide 3-dB 90° hybrid with its outputs connected to two HEB mixers. The HEB mixers employ novel membrane-beam layout. The waveguide full cross-section dimensions 60x120  $\mu\text{m}$ , 1.6-2.0 THz band.

## 5.1.2 HEB Mixer on Si Beams: Motivation and Concept

### A. Motivation

Traditional waveguide HEB mixers (and SIS mixers) are typically realized on quartz substrates. Crystalline quartz is an attractive material due to its low RF loss ( $\tan\delta=0.0002$ ), a low dielectric constant ( $\epsilon_r=3.8$ ), excellent thermal conductivity (Z-cut) as well as processing compatibility. Nevertheless, as the frequency approaches the THz domain, the thickness and size of the substrate becomes extremely small; that is required to avoid the substrate modes. In the traditional layout with a straight substrate at terahertz frequencies, this greatly complicates the handling and the assembly process as a result of the extremely reduced substrate dimensions and low mechanical strength of the substrate. The multi-pixel THz array receivers require many mixers and the way of the substrate mounting and handling becomes a critical issue. Thus a new approach to THz packaging of active substrate-based mixer is needed for implementing waveguide-based multipixel array receivers for terahertz spectroscopy.

Material such as silicon nitride exhibit high mechanical strength and relatively low dielectric constant ( $\epsilon_r=7$ ), which makes it attractive for waveguide mixers. Implementation of 1.4 THz and 1.9 THz NbTiN HEB mixers on silicon nitride membranes has been previously reported [110]. Nevertheless, for applications

where HEB mixer with large IF bandwidth is required, silicon nitride is not the optimum choice for beam material due to the relatively large phonon escape time from NbTiN film into the substrate. Typical bandwidths of HEB mixers on SiN membranes exhibit IF bandwidth up to 3 GHz [111].

Excellent mechanical properties of thin silicon membranes at cryogenic temperatures together with the low dielectric losses (high resistivity silicon) provide an opportunity for realizing HEB at THz frequencies. Previously, it has been proposed an alternative way of integration of substrate-based mixers by using beam-lead technology [112-114]. Beam leads provide good thermal and electrical connection to the device as well as mechanical support of the silicon chip while the circuits are usually packaged in split-block housing. However, once the beam-leaded mixer chip is mounted in the waveguide, it cannot be removed without significant damage to the beam leads. The substrate size for integration remains very small complicating installation and alignment of the substrate in the housing.

### *B. Concept*

In this work, an alternative HEB mixer layout based on Si beams is proposed, which employs a split-block waveguide design. The active devices are produced on a thin silicon membrane, oriented conventionally parallel to the E-field in the waveguide, supported by a bulk silicon half-frame  $\Pi$ -shaped at its ends. The beam itself contains the HEB device, RF chokes, an E-field probe and a high-impedance line. The  $\Pi$ -shaped bulk silicon frame, see Fig. 5.2, is left around the beam in order to ease the handling and contacting as well as providing a self alignment of the active device into the waveguide. The beam frame size is then removed from the RF embedding of the active component and could be selected to be large enough for handling, yet small enough to have negligible effect at the IF frequency.

In order to implement such layout we have to invent a suitable processing; for that we have chosen silicon-on-insulator (SOI) substrate, which incorporates five stacked layers of predefined thicknesses to allow precise vertical alignment of the beam. The structure can be integrated in a waveguide circuitry, e.g. following technique suggested [25, 26]. In order to accommodate the supporting frame and the beam, a special recess is considered around the waveguide area. This arrangement provides an additional advantage of straightforward sideways aligning in all directions as well as an easy replacement of the mixer chip from the mixer block if needed. Once secured in the recess, the IF and the ground pads in the support frame may then be wire bonded to an external IF circuit board and the mixer block for grounding, respectively.

An advantage of the presented approach should be a significant simplification in the mixer assembly and enhanced reliability of the electrical contacts made by, e.g., wire bonding. Using this mixer layout, an array receiver can be relatively quickly assembled with pre-characterized devices employing standard techniques such as wire bonding and soldering. The design also gives a possibility to access and remove individual devices without affecting the other elements of the array. This technique is also beneficial for single-element receivers as it facilitates rapid

prototyping and device replacement. The biggest advantage of the suggested approach is that it allows using the split-block technique in contrast to previously suggested approach in, e.g., [115], which uses end-piece configuration. The latter has obvious disadvantage of introducing “RF-leaking” split of the substrate channel in the waveguide.

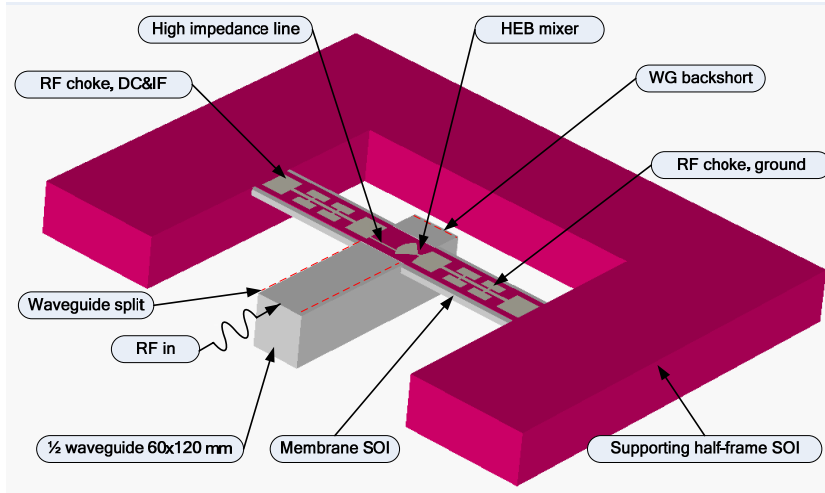


**Figure 5.2:** 3D model of the E-plane splitblock integrated HEB waveguide mixer on a Si beam with a support frame.

## 5.2 RF Design and Simulations

When constructing THz HEB mixers, it is important to design the mixer block in such way that the incoming waveguide mode is coupled to the hot-electron bolometer in a highly-efficient manner [116]. Most of the waveguide SIS and HEB mixers utilize planar E-field probes, to couple the EM wave in the waveguide to planar structure on the substrate produced by means of thin-film technology. As discussed in the previous section, the split-block technique has been employed. The advantages of this design is using of a non-radiating split of the waveguide, convenience of mounting the active component and making all necessary DC and IF connections in one of the halves for the chosen topology of the active component.

In order to define the dimensions and the critical margins of the design, extensive 3D electromagnetic simulations using a set of commercial software programs [117, 118] have been performed. The design was optimized for the best performance within the frequency range 1.6 - 2.0 THz.

Figure 5.3 shows the proposed layout for the HEB mixer for a 1.6-2.0 THz. In this arrangement, the substrate is placed parallel to the E-field in the waveguide. The silicon beam has dimensions of  $360 \mu\text{m} \times 50 \mu\text{m} \times 2 \mu\text{m}$ .

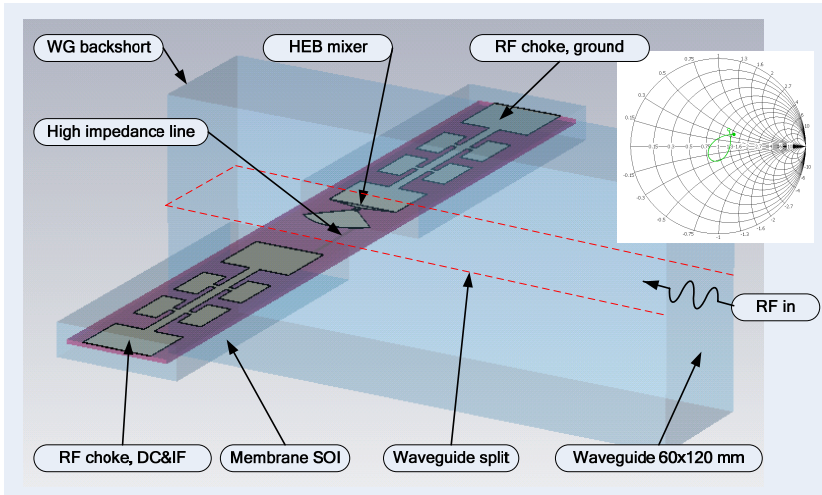


**Figure 5.3:** (a) 3D model and simulation results of the radial RF probe on a 2  $\mu\text{m}$  thick Si beam.

The RF signal coming from the waveguide is coupled to the mixer on the substrate through a radial probe patterned on the silicon beam. The geometry of the probe, i.e., the probe radius, has been optimized to give minimum reflections in the 1.6-2.0 THz band providing output impedance of 50  $\Omega$ . In the proposed design the RF probe is connected on its arc-side to another port via high impedance line that provides isolated port for IF and DC similar to suggested in [49].

Waveguide mixers as a rule use choke filters to efficiently block the leakage of the RF signal into the substrate channel and to provide virtual RF ground for high-frequency components placed onto the substrate. The choke structure, Fig. 5.4a, is used simultaneously for IF extraction and to supply a DC bias to the active component. The geometry of the hammer sections have been optimized to give maximum rejection in the 1.6-2.0 THz band. The performance of the hammer-type RF choke is illustrated in Fig. 5.4b, showing a rejection better than -40 dB in the whole band of interest.

In order to realize the balanced mixer a 3-dB 90°-hybrid is required. A waveguide branch-line coupler was chosen because of its compatibility with the split-block layout. The amplitude and phase imbalance at the outputs of a quadrature hybrid affect the LO noise rejection of the balanced mixer. Therefore, for the frequency range 1.6–2.0 THz the goal of the present work was to design a waveguide quadrature hybrid with an amplitude imbalance of  $\pm 1$  dB around the -3 dB and  $\pm 1^\circ$  phase imbalance. The reflection coefficient and isolation between the input ports are expected to be better than -20 dB. In addition, the acquired waveguide dimensions from the simulation must comply with the fabrication process developed at GARD [25].

A split-block type of hybrid, with equal-width branches [24] was chosen for the designed as it offers the advantage to have larger branch heights compared to classical designs [119]. Larger widths are important for the hybrid fabrication.

The height of the main waveguide sections was fixed at the full height ( $b = a/2$ ). In the 1.6-2 THz band this corresponds to  $120\ \mu\text{m} \times 60\ \mu\text{m}$  main waveguide dimensions. According to simulation results presented in Fig. 5.5, a hybrid with five branches is able to maintain an amplitude imbalance of  $\pm 1.5\ \text{dB}$  and  $90^\circ \pm 1^\circ$  phase difference over the full waveguide band.

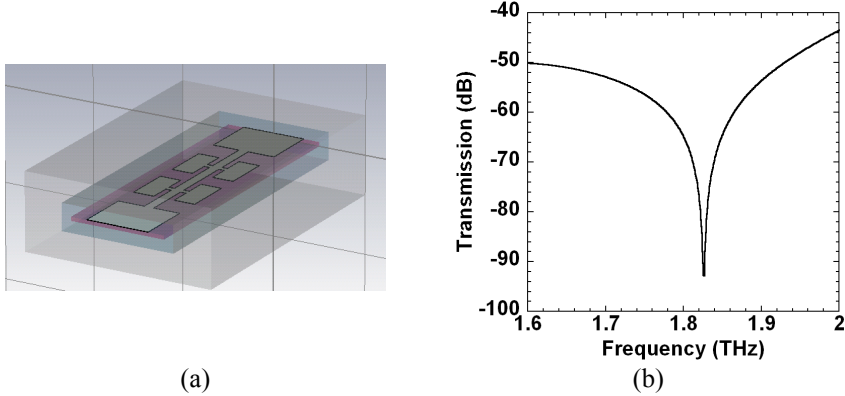


**Figure 5.4:** (a) Simulated RF choke on Si beam inside the waveguide channel. (b) Simulated performance of the RF hammer-type choke within the RF band.

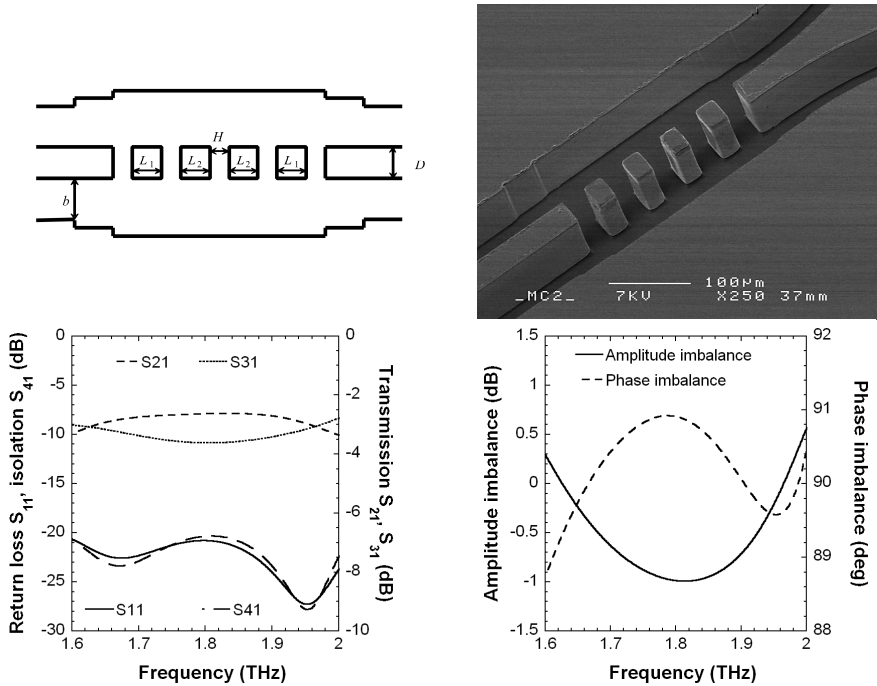


**Figure 5.5:** Simulation results of the five-branch waveguide hybrid coupler with equal-width branches. ( $H = 22\ \mu\text{m}$ ,  $L_1 = 33\ \mu\text{m}$ ,  $L_2 = 31\ \mu\text{m}$ ,  $D = 44\ \mu\text{m}$  and  $\Delta b = 6\ \mu\text{m}$ ).

### 5.1.4 Thermal Simulations

The ambient temperature of the HEB mixer is usually around 4K. In micromachined beams mechanical and thermal stresses induced during cooling/heating may lead to undesired deformation and even fracture of the beam. In addition, a small misplacement of the beam in the waveguide channel at THz frequencies may also de-tune the entire circuit or excite unwanted resonances. Therefore, important objective towards implementation of the proposed structure was to investigate the mechanical behaviour of the beam subjected to a temperature change from room temperature (300 K) down to LHe temperature (4.2 K), by performing thermo-mechanical simulations.

For this purpose, a 3D model was built, as shown in Fig. 5.6, using commercial finite element model (FEM) software [120]. For the simulation, the model resembles the SOI layer structure used for the fabrication. Table 5.1 shows the predicted total deformation as well as maximum principal stress for different beam thickness at 4.2 K.

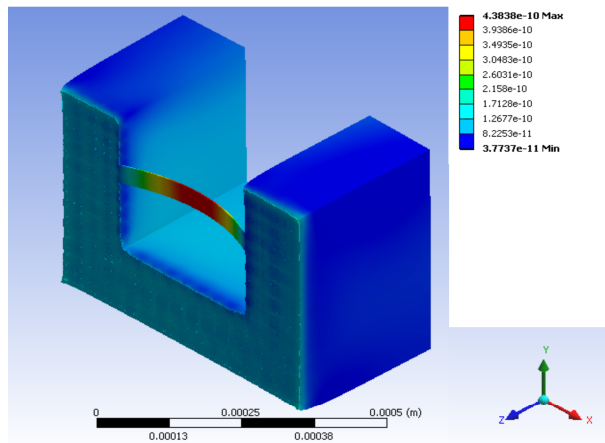


**Figure 5.6:** Simulation result of the total deformation of a 2  $\mu\text{m}$  thick silicon beam at 4.2 K. The deformation of the beam is largely exaggerated for better visualization.

**Table 5.1:** Simulation results for different Si beam thicknesses.

Si thickness ( $\mu\text{m}$ )	Total deformation (nm)	Maximum principal stress (MPa)
1	0.60	14.7
2	0.44	14.0
5	0.27	14.6
10	0.21	14.8
15	0.20	14.8

## 5.2 Results

In this section, results from the NbN ultra-thin films characterization as well as the DC measurement of the fabricated HEB devices are presented. Also, the integration of the manufactured balanced waveguide HEB mixer mount is shown.

### 5.2.1 Ultra-Thin NbN Films on Si and 3C-SiC/Si Substrates

Figure 5.7 shows the HRTEM images of epitaxial and polycrystalline NbN film grown on 3C-SiC/Si and Si substrate, respectively. The thickness of the film is 5 nm, as expected from the deposition rate calibration.

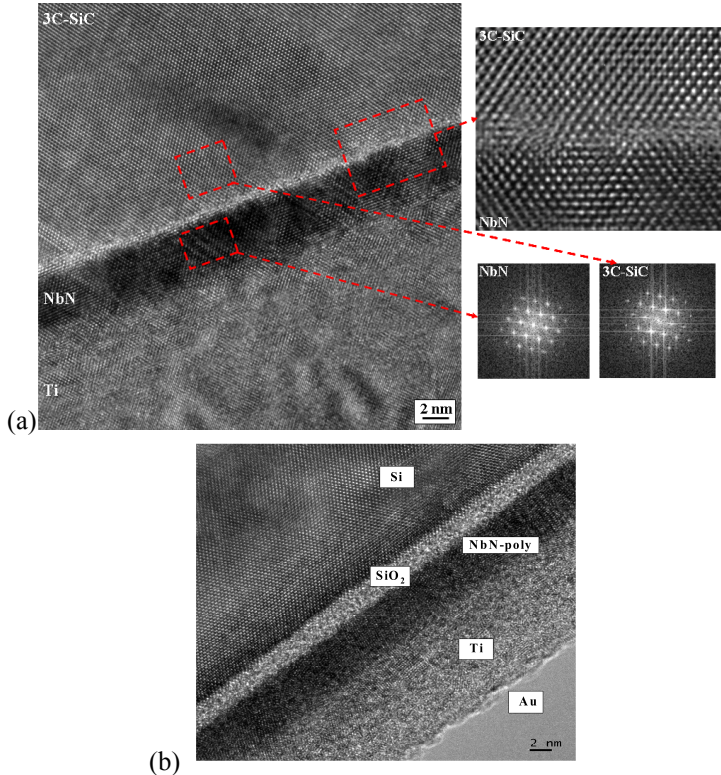


**Figure 5.7:** (a) Cross-sectional HRTEM images of epitaxial NbN film grown on 3C-SiC/Si substrate. To the right are enlargements of the indicated areas, presenting the NbN/3C-SiC interface and corresponding diffraction pattern calculated by Fourier transformation of the related image areas.  $T_c$  of the NbN film was 11.8 K. (b) Cross-sectional HRTEM image NbN film deposited on Si substrate.  $T_c$  of the film is 9.2 K.

### 5.2.2 HEB Devices on Si and 3C-SiC/Si Substrates

The enhanced crystalline properties of NbN films grown on 3C-SiC/substrate compared to those on Si and SOI substrates are clearly demonstrated in Fig. 5.8a. A difference in the critical temperatures of the plain NbN films of more than

2.5 K was observed. It has to be noted that no visible variation in  $T_c$  for the NbN films grown on Si and SOI substrate was seen. Measurements of the current-voltage characteristics of the fabricated HEB devices were done through a standard four-probe technique in a LHe dewar. The samples were glued on a fiberglass fixture and the individual HEB devices were connected through wire bonding. Due to the substantial difference in the crystal structure of the NbN films, a corresponding deviation in the measured critical currents was also present. The critical current values for devices on 3C-SiC overlayer were in the range 100-120  $\mu\text{A}$ , while for twice bigger devices made on SOI wafer, the critical currents were not higher than 90  $\mu\text{A}$ , Fig. 5.8. Complete DC characterization results on the HEB devices on epitaxial NbN can be found in *Paper E*.

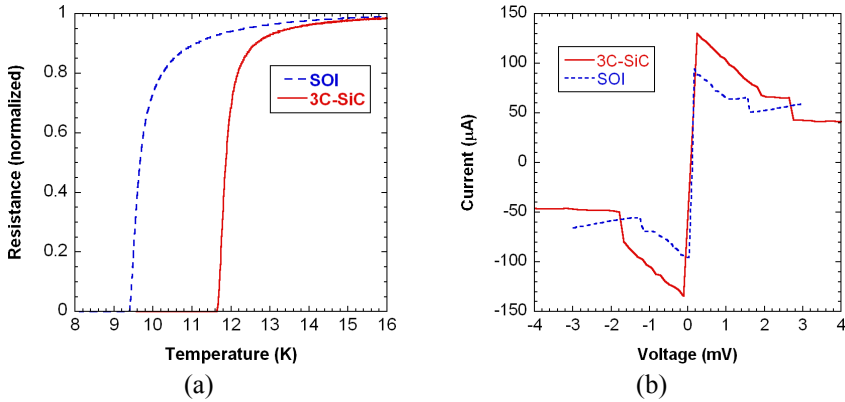
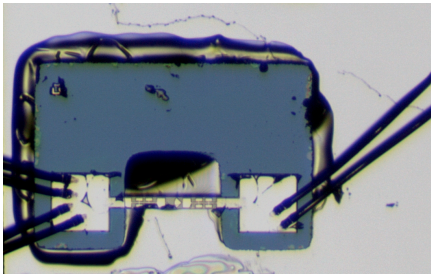


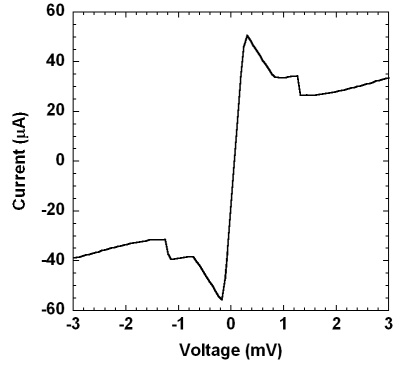
**Figure 5.8:** (a) Resistance-temperature dependence of the NbN film grown on 3C-SiC/Si and SOI substrates. (b) Current-voltage characteristics for two NbN HEB devices fabricated on 3C-SiC (solid) and SOI (dashed) substrates. The bridge width of the device made on SOI substrate is twice bigger ( $w = 1.6 \mu\text{m}$ ) than that made on 3C-SiC substrate.

### 5.2.3 HEB Devices on Si Beams

After the release of from the carrier wafer the individual devices were picked-up and placed in a gel-pack package as few devices were later taken for DC characterization. The latter ones were glued on a dedicated fixture and the individual devices were wire bonded for 4-probe DC measurements utilizing 25  $\mu\text{m}$  bond wires. Figure 5.9a shows the arrangement and a measured I-V curve. A slight decrease in the critical current compared to the initial tests before beam fabrication (see Fig. 5.8b). This behaviour could be attributed to degradation of the ultra-thin NbN films due to the high hard-baking temperature,  $\sim 200^\circ\text{C}$ , used for the protection resist layer. In one produced batch about 70 devices were successfully fabricated.



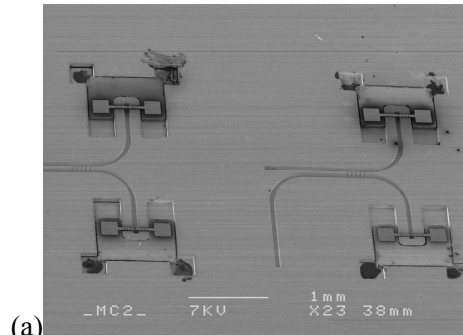
(a)



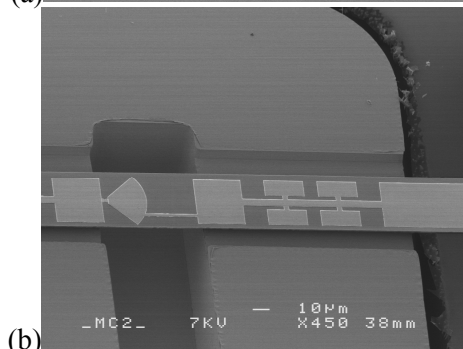
(b)

**Figure 5.9:** (a) An HEB device prepared for DC testing. (b) Current-voltage characteristics of the measured device.

SEM micrographs of the finished devices integrated in the copper waveguides are presented in Fig. 5.10.



(a)



(b)

**Figure 5.10:** SEM micrographs of (a) four integrated HEB devices with (b) a close view on one of the beams in the channel. Frame dimensions are  $900 \mu\text{m} \times 600 \mu\text{m} \times 60 \mu\text{m}$  and beam size is  $50 \mu\text{m} \times 360 \mu\text{m} \times 2 \mu\text{m}$ .

## 5.4 Summary

In Chapter 5 advancement towards balanced waveguide phonon-cooled HEB mixer for 1.6-2.0 THz were presented. Several technologies were merged for the development of such mixer: 1) NbN ultra-thin film deposition, 2) all-metal THz waveguide micromachining technology as well as 3) a novel HEB mixer chip made on thin Si beam was fabricated by means of Si micromachining. A demonstrator of the mixer was implemented and initial characterization results were presented.



## Chapter 6

# Future Directions and Summary of Appended Papers

### 6.1 Future Directions

The reported results in *Chapter 4* on the growth and properties of DC magnetron co-sputter deposited Nb<sub>3</sub>Al films suggest that obtaining terahertz Nb<sub>3</sub>Al-based SIS mixers/junctions is not too far from realization.

As a first step, a THz SIS mixer with Nb/Al-AIO<sub>x</sub>/Nb tunnel junctions and Nb<sub>3</sub>Al ground plane could be an interesting subject to investigate. Such mixer is supposed to benefit from the high-quality of the SIS junction and the significantly reduced RF loss around the junction, due to the higher energy gap of Nb<sub>3</sub>Al.

Second, direct studies on the superconducting gap of the Nb<sub>3</sub>Al films could be performed via hybrid junctions, made of Nb<sub>3</sub>Al bottom electrode and Nb top electrode. Of course, this requires development of high-quality tunnel barrier. This step would open the way towards implementation of Nb<sub>3</sub>Al-based junctions THz SIS mixers.

In addition, the results on epitaxial growth of Nb<sub>3</sub>Al on yttria-stabilized zirconia (YSZ) reveal quite attractive option to try a growth of ultra-thin Nb<sub>3</sub>Al, dedicated for HEB mixers.

The properties of the produced Nb<sub>3</sub>Al films might be also of interest for other applications with demand on high-current and high-magnetic field of operation.

The presented technology demonstrator for 1.6-2.0 THz balanced waveguide HEB mixer in *Chapter 5* confirms that the suggested concept can be realized both in theory and practice. However, as a complement to the performed DC measurements, further verification of the devices' RF performance is required. This fabrication technique could be also beneficial for other THz technologies such as SIS and Schottky-diode mixers.

The monocrystalline ultra-thin NbN films, grown on 3C-SiC substrates, have demonstrated potential to be used in practical HEB mixers. Measurements of the photoresponse of the fabricated HEB devices are necessary for the evaluation of the intrinsic mixer time constants. Certainly, RF characterization of an NbN HEB mixer made on 3C-SiC substrate is essential.

## 6.2 Summary of Appended Papers

### **Paper A: Nb<sub>3</sub>Al Thin Film Deposition for Low-Noise Terahertz Electronics**

Higher energy gap superconducting materials were always interesting for low-noise mixer applications such as superconductor-insulator-superconductor tunnel junctions (SIS) and hot-electron bolometer (HEB) used in sub-millimeter and terahertz parts of electro-magnetic spectrum. Here, we report a novel approach for producing Nb<sub>3</sub>Al thin film by co-sputtering from two confocally arranged Nb and Al dc-magnetrons onto substrate heated up to 830°C. Characterization of the deposited films revealed presence of the A15 phase and measured critical temperature was up to 15.7 K with the transition width 0.2-0.3 K for a 300 nm thick film. We measured the film critical magnetic field and studied influence of annealing on the film properties. We have investigated compositional depth profile of the deposited films by spectroscopy of reflected electrons.

*Author's contribution:* performed the Nb<sub>3</sub>Al thin film deposition and characterization (material and electrical); participated in the theory development; wrote the paper.

### **Paper B: The Influence of Aging and Annealing on the Properties of Nb/Al-AIO<sub>x</sub>/Nb Tunnel Junctions**

This paper presents results of our studies on aging and annealing properties of Nb/Al-AIO<sub>x</sub>/Nb junctions. We performed a long room temperature aging with subsequent annealing at different temperatures up to 250°C. A distinct change of the junctions' normal-state resistance has been observed. Aging at room temperature results in a slight decrease of the normal-state resistance combined with improved junction quality, characterised by a better subgap-to-normal resistance ratio. Annealing at moderate temperatures in air increases the normal-state resistance and leads to improvement of the junction quality followed by degradation at higher annealing temperatures. The increase in the junction quality after long-term aging at room temperature is attributed to relaxation of the internal junction structure and interfaces, thus, resulting in a lower density of interface traps. The deterioration at higher annealing temperatures could be a consequence of diffusion processes at the Al/Nb interface. We observe a sufficiently clear difference between the behaviour of preliminary aged and newly fabricated junctions after annealing: for the aged high-quality junction, the degradation was negligible up to temperatures of 200°C, while non-aged junctions show a much faster and abrupt degradation at lower annealing temperatures.

*Author's contribution:* performed the annealing experiments and electrical characterization; participated in the theory development; wrote the paper.

## **Paper C: Aging- and Annealing-Induced Variation of Nb/Al-AIO<sub>x</sub>/Nb Tunnel Junction Properties**

In this paper, we present studies of room temperature aging and annealing of Nb/Al-AIO<sub>x</sub>/Nb tunnel junctions with the size of a 2-3 μm<sup>2</sup> size. We observed a noticeable drop of junction normal resistance  $R_n$  unusually combined with increase of subgap resistance  $R_j$  as a result of aging. Variation of both  $R_n$  and  $R_j$  are subject to the junction size effect. An effect of aging history on the junction degradation after consequent annealing was discovered. Discussion and interpretation of the observed phenomena are presented in terms of structural ordering and reconstruction in the AIO<sub>x</sub> layer, driven by diffusion flows enhanced due to stress relaxation processes in the Al layer interfacing the AIO<sub>x</sub> layer.

*Author's contribution:* performed the annealing experiments and electrical characterization; participated in the theory development.

## **Paper D: Superconducting IF Biasing Circuit for Low-Noise Cryogenic Applications**

A planar superconducting circuit designed for use in low-noise cryogenic applications is presented. The circuit is a bias-T combined with a 4–8 GHz impedance matching circuitry, which employs entirely planar design with a novel layout. The proposed and tested circuitry is intended to be used with a SIS mixer and incorporates a double section transformer based on microstrip line technology with a total impedance transformation of 5:1 within the frequency band. One of the transformer sections employs a three-line coupled line, which also serves as a DC block capacitor. The microstrip lines were manufactured using superconducting Nb metallization, which provides a conduction loss-free solution at the operation temperature of 4 K. S-parameter measurements at 4 K temperature were performed and found to be in a good agreement with the simulations. The device measured return loss is better than –10 dB within the frequency band. Furthermore, the circuit was tested as a part of 385–500 GHz double sideband heterodyne SIS receiver demonstrating a flat noise temperature response of 80–90 K over the entire IF band of 4–8 GHz.

*Author's contribution:* performed the circuit design, fabrication and S-parameter measurements; wrote the paper.

## **Paper E: Growth and Characterization of Epitaxial Ultra-Thin NbN Films on 3C-SiC/Si Substrate for Terahertz Applications**

We report on electrical properties and microstructure of epitaxial thin NbN films grown on 3C-SiC/Si substrates by means of reactive magnetron sputtering. A complete epitaxial growth at the NbN/3C-SiC interface has been confirmed by means of high-resolution transmission electron microscopy (HRTEM) along with

x-ray diffractometry (XRD). Resistivity measurements of the films have shown that the superconducting transition onset temperature ( $T_c$ ) for the best specimen is 11.8 K. Using these epitaxial NbN films, we have fabricated submicron-size hot-electron bolometer (HEB) devices on 3C-SiC/Si substrate and performed their complete DC characterization. The observed critical temperature  $T_c = 11.3$  K and critical current density of about  $2.5 \text{ MA/cm}^2$  at 4.2 K of the submicron-size bridges were uniform across the sample. This suggests that the deposited NbN films possess the necessary homogeneity to sustain reliable hot electron bolometer device fabrication for THz mixer applications.

*Author's contribution:* performed the NbN thin film deposition, x-ray characterization, fabrication and DC measurements of the HEB devices; participated in the theory development; wrote the paper.

## **Paper F: A Technology Demonstrator for 1.6-2.0 THz Waveguide HEB Receiver with a Novel Mixer Layout**

In this paper, we present our studies on a technology demonstrator for a balanced waveguide hot-electron bolometer (HEB) mixer operating in the 1.6 - 2.0 THz band. The design employs a novel membrane-like layout for the HEB mixer combining several key technologies: all-metal THz waveguide micromachining, ultra-thin NbN deposition and a deep reactive ion etching of silicon-on-insulator (SOI) substrate to manufacture the HEB mixer with a novel layout. The presented in the paper novel mixer layout greatly facilitates the mixer chip handling, mounting and electrical interfacing, which, in our opinion, opens up a real prospective for building multi-pixel waveguide THz receivers. Such receivers could be of interest for APEX, CCAT telescopes and possible follow up of the Herschel HIFI.

*Author's contribution:* performed the circuit design, NbN thin film deposition, developed the beam process, performed the HEB device fabrication and DC measurements; participated in writing the paper.

## Appendix A: Crystallographic relationship between Nb<sub>3</sub>Al and Nb

The (110)Nb-plane and (210)Nb<sub>3</sub>Al-plane, with lattice constants  $a_{\text{Nb}} = 3.30 \text{ \AA}$  and  $a_{\text{Nb}_3\text{Al}} = 5.18 \text{ \AA}$ , respectively, are schematically shown in Fig. A1. The accommodation of Nb<sub>3</sub>Al crystal structure on top of Nb substrate is possible by accounting for the three directions marked as vectors (1), (2) and (3).

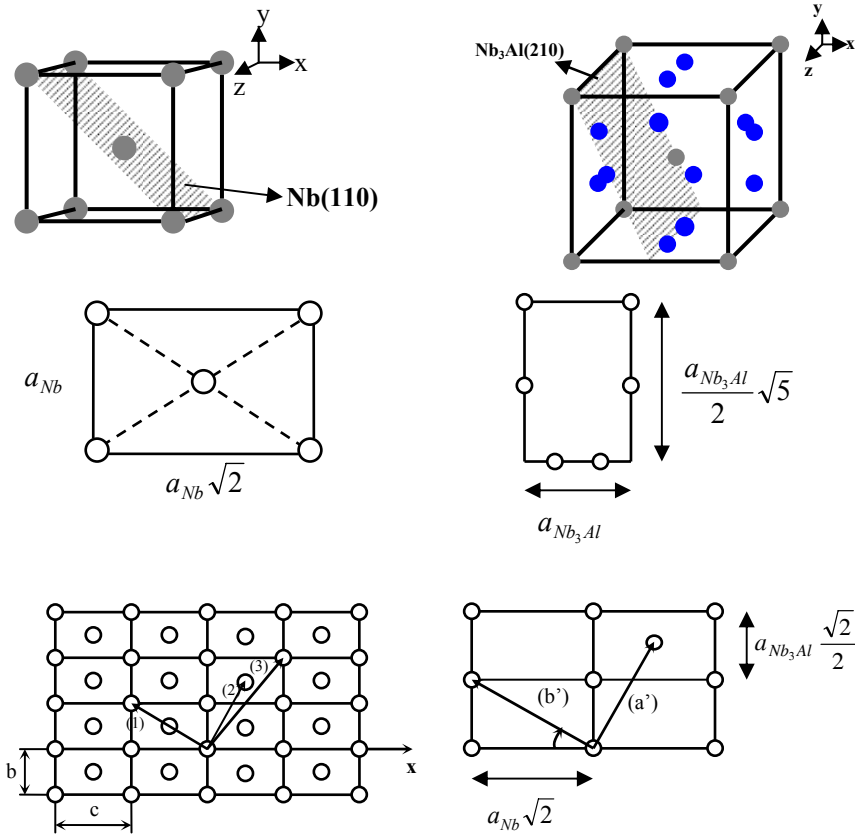


**Figure A1:** Schematic illustration of how the similar rotational symmetry of (110) and (210) planes can allow for low energy interfaces to exist on sets of (110)<sub>Nb</sub> and (210)<sub>Nb<sub>3</sub>Al</sub> planes.

The distances (1), (2) and (3) are:

$$(1) = \sqrt{b^2 + c^2} = \sqrt{a_{Nb}^2 + (a_{Nb}\sqrt{2})^2} = a_{Nb}\sqrt{3} = 5.716\text{\AA} \quad (\text{A.1})$$

$$(2) = \sqrt{\left(\frac{3}{2}b\right)^2 + \left(\frac{1}{2}c\right)^2} = \sqrt{\frac{9}{4}a_{Nb}^2 + \frac{2}{4}a_{Nb}^2} = \frac{a_{Nb}}{2}\sqrt{11} = 5.462\text{\AA} \quad (\text{A.2})$$

$$(3) = \sqrt{(2b)^2 + c^2} = \sqrt{4a_{Nb}^2 + 2a_{Nb}^2} = a_{Nb}\sqrt{6} = 8.083\text{\AA} \quad (\text{A.3})$$

Comparing the dimensions of Nb<sub>3</sub>Al(210) elementary cell with distances (1), (2) and (3) suggests that the Nb<sub>3</sub>Al(210) should be aligned with (1) and (2). Angle  $\alpha$  defines the angle, at which Nb<sub>3</sub>Al(210) is rotated in respect to Nb(110):

$$\cos \alpha = \frac{a_{Nb}\sqrt{2}}{a_{Nb}\sqrt{3}} = \sqrt{\frac{2}{3}} = \frac{\sqrt{6}}{3} \quad (\text{A.4})$$

In other words, there is a crystallographic relation between Nb(100) and Nb<sub>3</sub>Al(210) as

$$Nb\langle 110 \rangle \left( \frac{\sqrt{11}}{2}, \frac{\sqrt{6}}{2} \right) \mathbf{R} \arccos \frac{\sqrt{6}}{3}. \quad (\text{A.5})$$

## Appendix B: Abbreviations and notations

### Abbreviations

<b>2SB</b>	Sideband Separation
<b>AFM</b>	Atomic Force Microscope
<b>ALMA</b>	Atacama Large Millimeter Array
<b>APEX</b>	Atacama Pathfinder Experiment
<b>BCS</b>	Bardeen-Cooper-Schrieffer
<b>DC</b>	Direct Current
<b>DSB</b>	Double Sideband
<b>EBL</b>	Electron Beam Lithography
<b>GARD</b>	Group for Advanced Receiver Development
<b>HEB</b>	Hot Electron Bolometer
<b>IF</b>	Intermediate Frequency
<b>LHe</b>	Liquid Helium
<b>LNA</b>	Low-Noise Amplifier
<b>LO</b>	Local Oscillator
<b>LSB</b>	Lower Sideband
<b>PCB</b>	Printed Circuit Board
<b>RF</b>	Radio Frequency
<b>RIE</b>	Reactive Ion Etching
<b>RRR</b>	Residual Resistance Ratio
<b>RTA</b>	Rapid Thermal Annealing
<b>SEM</b>	Scanning Electron Microscope
<b>SHeFI</b>	Swedish Heterodyne Facility Instrument
<b>SIS</b>	Superconductor-Insulator-Superconductor
<b>SLC</b>	Single Layer Capacitor
<b>SOI</b>	Silicon-On-Insulator
<b>SPM</b>	Scanning Probe Microscope
<b>SRE</b>	Spectroscopy of Reflected Electrons
<b>SSB</b>	Single sideband
<b>TEM</b>	Transmission Electron Microscope
<b>USB</b>	Upper Sideband
<b>XRD</b>	X-Ray Diffraction
<b>YSZ</b>	Yttria Stabilized Zirconia

## Notations

$T_C$	Critical temperature
$D$	Diffusion coefficient
$\Phi_0$	Magnetic flux quantum,
$\xi_0$	Coherence length
$\lambda_L$	London penetration depth
$H_{c2}$	Upper critical field
$c$	Velocity of light, $2.998 \times 10^8 \text{ m s}^{-1}$
$e$	Electron charge, $1.602 \times 10^{-19} \text{ C}$
$k_B$	Boltzmann's constant, $1.38 \times 10^{-23} \text{ J K}^{-1}$
$h$	Planck's constant, $6.547 \times 10^{-34} \text{ J}\cdot\text{s}$
$\epsilon_0$	Permittivity of vacuum, $8.854 \times 10^{-12} \text{ F m}^{-1}$
$\delta_S$	Skin depth
$\mu_0$	Permeability of vacuum, $4\pi \times 10^{-7} \text{ H m}^{-1}$
$\rho_0$	Specific resistance
$a$	Lattice parameter
$l$	Mean free path
$v_F$	Fermi velocity
$\phi$	Potential barrier height

# Acknowledgements

First and foremost I would like to express my deep gratitude to Prof. Victor Belitsky, my examiner and supervisor, for the opportunity to start (and finish) my PhD studies at GARD. Thank you for the management, support and trust throughout this work. Your feedback has been indispensable for this thesis. Thank you, Victor!

I would like to thank my co-supervisors, Dr. Alexey Pavolotsky and Dr. Vincent Desmaris for their guidance, inspiration, encouragement and continued trust in me during these five years. I am very grateful for all the discussions, support and ideas, at any time, concerning the complicated world of micro and nanoprocessing. I have certainly learned many things from your great experience. It has been pleasure working with Dr. Denis Meledin and learn from his invaluable knowledge and skills concerning HEB mixers.

I am extremely lucky to be a part of such an amazing group like GARD, where professionalism and friendship are bonded quite tightly. I would like to thank all my friends and coworkers in the group, for whom it is incredibly difficult to rank by contribution to this work. Thank you, Olle, Bhushan, Doug, Erik, Gert, Hawal, Igor, Magnus, Mathias, Miro, Monica, Raquel, Sven-Erik and Vessen.

During this work, I certainly spent quite some time in the cleanroom. Therefore, I would like to thank the cleanroom personnel, who were doing everything to make my time less painful by providing support and licenses. Henrik Frederiksen and Göran Reivall are acknowledged for the great help with the installation and support of our precious sputtering equipment. My appreciation goes also to Göran Pettersson, Bengt Nilsson, Johan Andersson, Mats Hagberg, Kaija Matikainen and Jonh Halonen.

Dr. Alexey Kalabukhov is acknowledged for his great help with critical field measurements and very fruitful discussions concerning this work. Thanks to Dr. Zonghe Lai and the TEM images he shot, it was possible to evaluate very precious information regarding the film structure. I would like to thank also our collaborators from Linköping University, Prof. Eric Janzén and Assoc. Prof. Anne Henry, for the 3C-SiC material. I am also grateful to Prof. J. Woltersdorf and Dr. E. Pippel from MPI Halle, Germany for the wonderful TEM images. Dr. A. Lubenchenko is acknowledged for the SRE measurements.

I should not forget all my friends here in Sweden, in Bulgaria and eventually around the world, whose friendship have always kept my spirit high.

Very and many special thanks go to my lovely fiancée and sambo Aleksandra for her love and support.

Finally, I will always be grateful to my family for their endless love and support. To you I dedicate this thesis!

This work was supported by the Swedish Research Council (VR) through a Project Grant No. 2005-3545 and the European Commission Framework Programme 7, Advanced Radio Astronomy in Europe, AMSTAR+, Grant No. 227290.



# References

- [1] S. C. Mukhopadhyay, R. Y. M. Huang, and G. Chattopadhyay, "Submillimeter-Wave Coherent and Incoherent Sensors for Space Applications," in *Sensors*. vol. 21: Springer Berlin Heidelberg, 2008, pp. 387-414.
- [2] B. Ferguson and X. C. Zhang, "Materials for THz science and technology," *Nature Materials*, vol. 1, pp. 26-33, 2002.
- [3] C. P. P. Jr., *Handbook of superconductivity*. San Diego, CA, USA: University of South Carolina, 2000.
- [4] J. R. Waldram, "The Josephson current in weakly coupled superconductors," *Rep. Prog. Phys.*, vol. 39, pp. 751-821, 1976.
- [5] V. V. Schmidt, *The physics of superconductors: Introduction to fundamentals and applications*. New York: Springer, 1997.
- [6] M. Tinkham, *Introduction to superconductivity*, 2 ed. New York: McGraw-Hill, 1996.
- [7] J. R. Tucker and M. J. Feldman, "Quantum detection at millimeter wavelengths," *Rev. Mod. Phys.*, vol. 57, pp. 1055-1113, 1985.
- [8] D. M. Pozar, *Microwave engineering*, 3rd ed.: John Wiley & Sons, Inc., 2005.
- [9] S. A. Maas, *Microwave mixers*. Boston: Artech House, 1993.
- [10] P. H. Siegel, "THz technology: An overview," *Int. J. High Speed Electron. Syst.*, vol. 13, pp. 351-394, 2003.
- [11] A. H. Dayem and R. J. Martin, "Quantum interaction of microwave radiation with tunnelling between superconductors," *Phys Rev. Lett.*, vol. 8, pp. 246-248, 1962.
- [12] C. J. Adkins, "Multi-particle tunnelling between superconductors," *Rev. Mod. Phys.*, vol. 36, pp. 211-213, 1964.
- [13] K. H. Gundlach and M. Schicke, "SIS and bolometer mixers for terahertz frequencies," *Supercond. Sci. Technol.*, vol. 13, pp. 171-187, 2000.
- [14] A. Karpov, D. Miller, F. Rice, J. A. Stern, B. Bumble, H. G. LeDuc, and J. Zmuidzinas, "Low noise 1 THz-1.4 THz mixers using Nb/Al-AlN/NbTiN SIS junctions," *IEEE Trans. Appl. Supercond.*, vol. 17, pp. 343-346, 2007.
- [15] E. M. Gershenzon, M. E. Gershenzon, G. N. Gol'tsman, A. M. Lyul'kin, and A. D. Semenov, "Electron-phonon interaction in ultrathin Nb films," *Sov. J. JETP*, vol. 70, pp. 505-511, 1990.
- [16] W. Zhang, J. R. Gao, P. Khosropanah, T. Bansal, T. M. Klapwijk, W. Miao, and S. C. Shi, "NbN hot electron bolometer mixer at 5.3 THz," *Proc. SPIE - Int. Soc. Opt. Eng.*, vol. 7741, p. 77411B, 2010.
- [17] P. Santhanam and D. E. Prober, "Inelastic electron scattering mechanisms in clean aluminum films," *Phys. Rev. B*, vol. 29, pp. 3733-3736, 1984.
- [18] Y. P. Gousev, G. N. Gol'tsman, A. D. Semenov, E. M. Gershenzon, R. S. Nebosis, M. A. Heusinger, and K. F. Renk, "Broadband ultrafast superconducting NbN detector for electromagnetic radiation," *J. Appl. Phys.*, vol. 75, pp. 3695-3697, 1994.
- [19] E. M. Gershenzon, G. N. Gol'tsman, Y. P. Gousev, A. I. Elant'ev, and A. D. Semenov, "Electromagnetic radiation mixer based on electron heating in resistive state of superconductive Nb and YBaCuO films," *IEEE Trans. Magn.*, vol. 27, pp. 1317-1320, 1991.
- [20] D. E. Prober, "Superconducting terahertz mixer using a transition-edge microbolometer," *Appl. Phys. Lett.*, vol. 62, pp. 2119-2121, 1993.
- [21] A. V. Sergeev and M. Y. Reizer, "Photoresponse mechanisms of thin superconducting films and superconducting detectors," *Int. J. Mod. Phys. B*, vol. 10, pp. 635-667, 1996.
- [22] A. D. Semenov, G. N. Gol'tsman, and R. Sobolewski, "Hot-electron effect in superconductors and its application for radiation sensors," *Supercond. Sci. Technol.*, vol. 15, pp. R1-R16, 2002.
- [23] K. S. Il'in, M. Lindgren, M. Currie, A. D. Semenov, G. N. Gol'tsman, R. Sobolewski, S. I. Cherednichenko, and E. M. Gershenzon, "Picosecond hot-electron energy relaxation in NbN superconducting photodetectors," *Appl. Phys. Lett.*, vol. 76, pp. 2752-2753, 2000.
- [24] J. W. Kooi, "Advanced receivers for submillimeter and far infrared astronomy," 2008.

- [25] V. Desmaris, D. Meledin, A. Pavolotsky, R. Monje, and V. Belitsky, "All-metal micromachining for the fabrication of sub-millimetre and THz waveguide components and circuits," *J. Micromech. Microeng.*, vol. 18, p. 095994, 2008.
- [26] D. Meledin, A. Pavolotsky, V. Desmaris, I. Lapkin, C. Risacher, V. P. Robles, D. Henke, O. Nyström, E. Sundin, D. Dochev, M. Pantaleev, M. Fredrixon, M. Strandberg, B. Voronov, G. Gol'tsman, and V. Belitsky, "A 1.3 THz balanced waveguide HEB mixer for the APEX telescope," *IEEE Trans. Microwave Theory Tech.*, vol. 57, pp. 89-98, 2009.
- [27] J. V. Gates, M. A. Washington, and M. Gurvitch, "Critical current uniformity and stability of Nb/Al-oxide-Nb Josephson junctions," *J. Appl. Phys.*, vol. 55, pp. 1419-1421, 1984.
- [28] K. Hinode, T. Satoh, S. Nagasawa, and M. Hidaka, "Hydrogen-inclusion-induced critical current deviation of Nb-Al/AlO<sub>x</sub>-Nb Josephson junctions in superconductor integrated circuits," *IEEE Trans. Appl. Supercond.*, vol. 19, pp. 131-134, 2009.
- [29] K. Hinode, T. Satoh, S. Nagasawa, and M. Hidaka, "Origin of hydrogen-inclusion-induced critical current deviation of Nb-Al/AlO<sub>x</sub>-Nb Josephson junctions," *J. Appl. Phys.*, vol. 107, p. 073906, 2010.
- [30] T. Lehnert, D. Billon, C. Grassl, and K. H. Gundlach, "Thermal annealing properties of Nb-Al/AlO<sub>x</sub>-Nb tunnel junctions," *J. Appl. Phys.*, vol. 72, 1992.
- [31] S. Morohashi, Y. Kataoka, T. Imamura, and S. Hasuo, "Secondary ion mass spectrometry study for Josephson junction with Nb/Al-AlO<sub>x</sub>/Nb structure," *Appl. Phys. Lett.*, vol. 62, pp. 1164-1166, 1993.
- [32] A. Oliva and R. Monaco, "Annealing properties of high quality Nb/Al-AlO<sub>x</sub>/Nb tunnel junctions," *IEEE Trans. Appl. Supercond.*, vol. 4, p. 25, 1994.
- [33] T. Shiota, T. Imamura, and S. Hasuo, "Fabrication of high quality Nb/Al-AlO<sub>x</sub>/Nb Josephson junctions: III - Annealing stability of AlO<sub>x</sub> tunnelling barriers," *IEEE Trans. Appl. Supercond.*, vol. 2, pp. 1419-1421, 1992.
- [34] S. K. Tolpygo and D. Amparo, "Fabrication-process-induced variations of Nb-Al/AlO<sub>x</sub>-Nb Josephson junctions in superconductor integrated circuits," *Supercond. Sci. Technol.*, vol. 23, p. 034024, 2010.
- [35] M. Gurvitch, M. A. Washington, and H. A. Huggins, "High quality Josephson tunnel junctions utilizing thin aluminium layers," *Appl. Phys. Lett.*, vol. 42, pp. 472-474, 1983.
- [36] T. Imamura, T. Shiota, and S. Hasuo, "Fabrication of high quality Nb/AlO<sub>x</sub>-Al/Nb Josephson junctions: I – sputtered Nb film for junction electrodes," *IEEE Trans. Appl. Supercond.*, vol. 2, pp.??, 1992.
- [37] M. Gurvitch, J. M. Rowell, H. A. Huggins, M. A. Washington, and T. A. Fulton, "Nb Josephson tunnel junctions with thin layer of Al near the barrier," *IEDM*, vol. 81, pp. 115-117, 1981.
- [38] V. Belitsky, I. Lapkin, V. Vassilev, R. Monje, A. B. Pavolotsky, D. Meledin, D. Henke, O. Nyström, V. Desmaris, C. Risacher, M. Svensson, M. Olberg, E. Sundin, M. Fredrixon, D. Dochev, S.-E. Ferm, and H. Olofsson, "Facility Heterodyne Receiver for the Atacama Pathfinder Experiment Telescope," in *Joint 32<sup>nd</sup> Int. Conf. Infrared Millimeter Waves and 15<sup>th</sup> Int. Conf. Terahertz Electronics* Cardiff, UK, 2007.
- [39] R. R. Monje, V. Belitsky, V. Vassilev, A. B. Pavolotsky, and I. Lapkin, "A 385-500 GHz SIS mixer for APEX telescope," in *SPIE Int. Soc. Opt. Eng.*, 2006.
- [40] A. B. Ermakov, S. V. Shitov, A. M. Baryshev, V. P. Koshelets, and W. Luinge, "A data acquisition system for test and control of superconducting integrated receivers," *IEEE Trans. Appl. Supercond.*, vol. 11, pp. 840-843 2001.
- [41] J. R. Nesbitt and A. F. Hebard, "Time-dependent glassy behaviour of interface states in Al-AlO<sub>x</sub>-Al tunnel junctions," *Phys. Rev. B*, vol. 75, p. 195441, 2007.
- [42] P. J. Koppinen, L. M. Väistö, and I. J. Maasilta, "Complete stabilization and improvement of the characteristics of tunnel junctions by thermal annealing," *Appl. Phys. Lett.*, vol. 90, p. 053503, 2007.
- [43] P. C. Snijders, L. P. H. Jeurgens, and W. G. Sloof, "Structural ordering of ultra-thin, amorphous aluminium-oxide films," *Surface Science*, vol. 589, pp. 98-105, 2005.
- [44] F. Reichel, L. P. H. Jeurgens, G. Richter, and E. J. Mittemeijer, "Amorphous versus crystalline state for ultrathin Al<sub>2</sub>O<sub>3</sub> overgrowths on Al substrates," *J. Appl. Phys.*, vol. 103, p. 093515, 2008.
- [45] J. W. Kooi, F. Rice, G. Chattopadhyay, S. Sundarum, S. Weinreb, and T. G. Phillips, "Regarding the IF output conductance of SIS tunnel junctions and the integration with

- cryogenic InP MMIC amplifiers," *Proc. 10th Int. Symp. Space THz Technol.*, pp. 100-117, 1999.
- [46] V. Belitsky, Private communication.
- [47] V. Vassilev, *Development of a sideband separating SIS mixer technology for mm-wavelengths*: Doctoral thesis, Chalmers University of Technology, 2003.
- [48] V. Vassilev, V. Belitsky, C. Risacher, I. Lapkin, A. Pavolotsky, and E. Sundin, "A Sideband Separating Mixer for 85-115 GHz," *IEEE Microwave Wireless Comp. Lett.*, vol. 14, pp. 256-258, 2004.
- [49] C. Risacher, V. Belitsky, V. Vassilev, I. Lapkin, and A. Pavolotsky, "A 275-370 GHz receiver SIS Mixer with novel probe structure," *Int. J. Infrared and Millimeter Waves*, vol. 26, pp. 867-879, 2005.
- [50] J. W. Kooi, A. Kovacs, M. C. Summer, G. Chattopadhyay, R. Ceria, D. Miller, B. Bumble, H. G. LeDuc, J. A. Stern, and T. G. Phillips, "A 275-425-GHz tunerless waveguide receiver based on AlN-barrier SIS technology," *IEEE Trans. Microwave Theory Tech.*, vol. 55, pp. 2086-2096, 2007.
- [51] V. K. Tripathi, Y. K. Chin, and H. Lee, "Interdigital multiple coupled microstrip DC blocks," in *Proc. 12th European Microwave Conference*, pp. 632-636, 1982.
- [52] Agilent Technologies, *ADS*, 2008.
- [53] Agilent Technologies, *EMDS*, 2000.
- [54] R. Monje, V. Belitsky, V. Vassilev, A. Pavolotsky, I. Lapkin, V. Desmaris, D. Meledin, D. Henke, and D. Dochev, "A 0.5 THz sideband separation SIS mixer for APEX Telescope," in *19th International Symposium on Space Terahertz Technology*, 2008.
- [55] B. Billade, V. Belitsky, A. Pavolotsky, I. Lapkin, R. Monje, V. Vassilev, and J. W. Kooi, "ALMA Band 5 (163-211 GHz) sideband separating mixer design," *Proc. 19th Int. Symp. Space THz Technol.*, pp. 250-252, 2008.
- [56] E. M. Gershenzon, M. E. Gershenzon, G. N. Gol'tsman, A. D. Semenov, and A. V. Sergeev, "Wide-band high-speed Nb and YBaCuO detectors," *IEEE Trans. on Magnetics*, vol. 27, pp. 2836-2839, 1991.
- [57] K. Tanabe and et al., "Nb-based A15 compound Josephson tunnel junctions fabricated using a CF<sub>4</sub> cleaning process: II. Properties of magnetron-sputtered Nb<sub>3</sub>X(X=Al,Ge) films," *J. Appl. Phys.*, vol. 61, pp. 373-383, 1987.
- [58] E. A. Wood, "Beta-wolfram structure of compounds between transition elements and aluminium, gallium and antimony," *Acta Crystall.*, vol. 11, pp. 604-606, 1958.
- [59] E. Corenzvit, "Superconductivity of Nb<sub>3</sub>Al," *J. Phys. Chem. Solids*, vol. 9, p. 93, 1959.
- [60] A. Godeke, "A review of the properties of Nb<sub>3</sub>Sn and their variation with A15 composition, morphology and strain state," *Supercond. Sci. Technol.*, vol. 19, pp. R68-R80, 2006.
- [61] J. L. Jorda, R. Flükiger, and J. Muller, "A new metallurgical investigation of the Niobium-Aluminium system," *J. Less-Common Met.*, vol. 75, pp. 227-239, 1980.
- [62] V. N. Svechnikov, "The constitution diagram of a system Niobium-Aluminum," *Metallofizika*, vol. 22, pp. 54-61, 1968.
- [63] C. E. Lundin and A. S. Yamamoto, "The equilibrium phase diagram, Niobium(Columbium)-Aluminum," *Trans. Met. Soc. AIME*, vol. 236, pp. 863-872, 1966.
- [64] F. Buta, "Phase evolution and superconducting properties of Nb-Al superconductors processed by a rapid heating/quenching method," The Ohio State University, 2003, pp. 12-16.
- [65] Y. V. Levinskiy, "Metall-gas phase diagrams," *Metallurgiya*, pp. 239-261, 1975.
- [66] M. Salez, J. A. Stern, W. R. McGrath, and H. G. LeDuc, "NbN mixers and tuning circuits for 630 GHz: design and preliminary measurements," in *Proc. 6th Int. Symp. on Space Terahertz Technology*, California Institute of Technology, Pasadena, USA, 1995, pp. 103-116.
- [67] T. Ando, Y. Takahashi, M. Sugimoto, M. Noshi, H. Tsuji, Y. Yamada, and M. Nagata, "First results of stress effects on I<sub>c</sub> of Nb<sub>3</sub>Al cable in conduit fusion superconductors," *IEEE Trans Applied Superconductivity*, vol. 3, pp. 1342-1345, 1993.
- [68] T. Kiyoshi and et al., "Development of an inner coil for a 1 GHz NMR magnet," *Japan Soc. Appl. Phys.*, vol. 67, pp. 431-434, 1998.
- [69] B. A. Glowacki, "Niobium aluminide as a source of high-current superconductors," *Intermetallics*, vol. 7, pp. 117-140, 1999.

- [70] J. Kwo and et al., "Nb<sub>3</sub>Al thin film synthesis by electron beam coevaporation," *J. Appl. Phys.*, vol. 51, pp. 1726-1732, 1980.
- [71] J. R. Gavaler and et al., "Sputtering techniques for controlling composition of thin films of high-T<sub>c</sub> superconducting compounds," *J. Vac. Sci. Technol.*, vol. 8, pp. 180-183, 1971.
- [72] K. Tanabe, "Synthesis of Nb<sub>3</sub>Al thin films by magnetron sputtering," *Jap. J. Appl. Phys.*, vol. 20, pp. L359-L362, 1981.
- [73] K. Agatsuma and e. al., "Nb<sub>3</sub>Al thin films made by single RF magnetron sputtering target," *Physica C*, vol. 372-376, pp. 1378-1381, 2002.
- [74] J. R. Gavaler and et al., "Oxygen distribution in sputtered Nb-Ge films," *Appl. Phys. Lett.*, vol. 28, pp. 237-239, 1976.
- [75] C. T. Wu, "High-rate magnetron sputtering of high T<sub>c</sub> Nb<sub>3</sub>Sn films," *J. Vac. Sci. Technol.*, vol. 14, pp. 134-137, 1977.
- [76] K. Barmak and et al., "Phase formation sequence for the reaction of multilayer thin films of Nb/Al," *J. Appl. Phys.*, vol. 67, pp. 7313-7322, 1990.
- [77] Y. Im and et al., "Nb<sub>3</sub>Al formation in sputtered-deposited Nb/Al multilayer samples," *J. Less Common Metals*, vol. 139, pp. 87-95, 1988.
- [78] J. M. Vandenberg and et al., "Reactive diffusion and superconductivity of Nb<sub>3</sub>Al multilayer films," *J. Appl. Phys.*, vol. 58, pp. 618-619, 1985.
- [79] E. I. Tochitskii and et al., "Superconductivity of thin molybdenum-rhenium films prepared by the method of pulsed laser deposition," *Phys. Met. Metallogr.*, vol. 67, pp. 1080-1083, 1989.
- [80] AJA International Inc., *ATC ORION 5 UHV*, 2006.
- [81] T. Takeuchi, N. Banno, T. Fukuzaki, and H. Wada, "Large improvement in high field critical current densities of Nb<sub>3</sub>Al conductors by the transformation-heat-based up-quenching method," *Supercond. Sci. Technol.*, vol. 13, pp. L11-L14, 2000.
- [82] A. Kakuchi, Y. Iijima, and K. Inoue, "Nb<sub>3</sub>Al conductor fabricated by DRHQ (Double Rapidly-Heating/Quenching) process," *IEEE Trans. Appl. Supercond.*, vol. 11, pp. 3968-3971, 2001.
- [83] Veeco Metrology Group, *Scanning probe microscopy training notebook* vol. Cleanroom edition 3: Digital Instruments, Veeco Metrology Group, 1998.
- [84] V. P. Afanas'ev, A. V. Lubenchenko, M. V. Lukashevsky, M. Norell, and A. B. Pavolotsky, "Study of Al/Nb interface by spectroscopy of reflected electrons," *J. Appl. Phys.*, vol. 101, pp. 064912-1-064912-6, 2007.
- [85] V. P. Afanas'ev, A. V. Lubenchenko, S. D. Fedorovich, and A. B. Pavolotsky, "Reflection of keV-energy electrons from multilayer surfaces," *Tech. Phys.*, vol. 47, pp. 1444-1452, 2002.
- [86] Lake Shore Cryotronics Inc.
- [87] C. D. Bencher, L. Murugesu, K. T. V. Rao, and R. O. Ritchie, "Phase transformations in in situ Nb-reinforced Nb<sub>3</sub>Al intermetallic composite," *Intermetallics*, vol. 4, pp. 23-29, 1996.
- [88] T. P. Orlando, E. J. M. Jr., S. Foner, and M. R. Beasley, "Critical fields, paramagnetic limiting, and material parameters of Nb<sub>3</sub>Sn and V<sub>3</sub>Si," *Phys. Rev. B*, vol. 19, pp. 4545-4561, 1979.
- [89] S. Kuriki, A. Yoshida, and H. Konishi, "Vortex behavior in Nb<sub>3</sub>Ge microbridges," *J. Low Temp. Phys.*, vol. 51, pp. 149-163, 1983.
- [90] A. I. Larkin and Y. N. Ovchinnikov, "Nonlinear conductivity of superconductors in the mixed state," *Sov. Phys. JETP*, vol. 38, 1974.
- [91] H. Wiesmann, M. Gurvitch, A. K. Ghosh, H. Lutz, O. F. Kammerer, and M. Strongin, "Estimate of density-of-states changes with disorder in A15 superconductors," *Phys. Rev. B*, vol. 17, pp. 122-125, 1978.
- [92] P. B. Allen, W. E. Pickett, K. M. Ho, and M. L. Cohen, "Anomalous resistivities of A15 metals - insights from band theory," *Phys. Rev. Lett.*, vol. 40, pp. 1532-1535, 1978.
- [93] D. W. Floet, J. R. Gao, T. M. Klapwijk, and P. A. J. d. Korte, "Thermal time constant of Nb diffusion-cooled superconducting hot-electron bolometer mixers," *IEEE Trans. Appl. Supercond.*, vol. 11, pp. 187-190, 2001.
- [94] M. Finkel, Y. Vachtomin, S. Antipov, V. Drakinskyi, N. Kaurova, B. Voronov, and G. Gol'tsman, "Gain bandwidth and noise temperature of NbTiN HEB mixer," in *14th Int. Symp. on Space Terahertz Technology*, 2003.

- [95] K. Tanabe and O. Michikami, "Self-epitaxial deposition of high- $T_c$  Nb<sub>3</sub>Al thin films," *J. Appl. Phys.*, vol. 56, pp. 3261-3270, 1984.
- [96] A. H. Dayem, T. H. Geballe, R. B. Zubeck, A. B. Hallak, and J. G. W. Hull, "Epitaxial growth of Nb<sub>3</sub>Ge on Nb<sub>3</sub>Ir and Nb<sub>3</sub>Rh," *J. Phys. Chem. Solids*, vol. 39, pp. 529-538, 1978.
- [97] R. D. Feldman, "Growth of Al<sub>15</sub> Nb-Si by epitaxy and composition grading," *Thin Solid Films*, vol. 87, pp. 243-258, 1982.
- [98] H. Asano, K. Tanabe, Y. Katoh, and O. Michikami, "Epitaxial growth of superconducting Nb<sub>3</sub>Ge films on YSZ single-crystal substrates," *Jap. J. Appl. Phys.*, vol. 27, pp. 35-39, 1989.
- [99] C. Pascual and P. Durán, "Subsolidus phase equilibria and ordering in the system ZrO<sub>2</sub>-Y<sub>2</sub>O<sub>3</sub>," *J. American Ceramic Soc.*, vol. 66, pp. 23-27, 1983.
- [100] M. Yoshimura, "Phase Stability of Zirconia," *Ceramic Bulletin*, vol. 67, pp. 1950-1955, 1988.
- [101] [Online], Available: [www.crystec.de](http://www.crystec.de).
- [102] H. Yi, R. Wang, H. Li, Y. Chen, B. Yin, X. Ron, and L. Li, "In situ epitaxial growth of the GdBa<sub>2</sub>Cu<sub>3</sub>O<sub>7</sub> superconducting thin films on (100) ZrO<sub>2</sub> by magnetron sputtering," *Appl. Phys. Lett.*, vol. 56, pp. 2231-2233, 1990.
- [103] T. Hata and et al., "Yttria-stabilized zirconia (YSZ) heteroepitaxially grown on Si substrates by reactive sputtering," *Vacuum*, vol. 59, pp. 381-389, 2000.
- [104] G. de Lange, "Development of the HIFI band 3 and 4 mixer units," *Proc. SPIE Int. Soc. Opt. Eng.*, vol. 5498, pp. 267-277, 2004.
- [105] G. H. Tan, "The ALMA front ends: an overview," in *Proc. 19<sup>th</sup> Int. Symp. Space Terahertz Technol.* Groningen, 2008.
- [106] S. Cherednichenko, V. Drankinskiy, T. Berg, P. Khosropanah, and E. Kollberg, "Hot-electron bolometer terahertz mixers for the Hershel Space Observatory," *Rev. Sci. Inst.*, vol. 79, p. 034501, 2008.
- [107] P. Khosropanah, J. R. Gao, W. M. Laauwen, M. Hajenius, and T. M. Klapwijk, "Low noise NbN hot electron bolometer mixer at 4.3 THz," *Appl. Phys. Lett.*, vol. 91, p. 221111, 2007.
- [108] D. P. Marrone, R. Blundell, E. Tong, S. N. Paine, D. Loudkov, J. H. Kawamura, D. Lühr, and C. Barrientos, "Observations in the 1.3 and 1.5 THz atmospheric windows with the receiver lab telescope," in *16<sup>th</sup> Int. Symp. Space Terahertz Technol.* Göteborg, Sweden, 2005.
- [109] E. Tong, J. Kawamura, D. Marrone, D. Loudkov, S. Paine, R. Blundell, C. Barrientos, and D. Lühr, "A 1.5 THz hot electron bolometer receiver for ground-based terahertz astronomy in northern Chile," *Proc. SPIE*, vol. 6373, 2006.
- [110] P. P. Muñoz, S. Bedorf, M. Brandt, T. Tils, N. Honingh, and K. Jacobs, "THz waveguide mixers with NbTiN HEBs on silicon nitride membranes," *IEEE Microwave Wireless Comp. Lett.*, vol. 16, pp. 606-608, 2006.
- [111] S. Cherednichenko, V. Drankinskiy, J. Baubert, J.-M. Krieg, B. Voronov, G. Gol'tsman, and V. Desmaris, "Gain bandwidth of NbN hot-electron bolometer terahertz mixers on 1.5 μm Si<sub>3</sub>N<sub>4</sub>/SiO<sub>2</sub> membranes," *J. Appl. Phys.*, vol. 101, p. 124508, 2007.
- [112] R. B. Bass, J. C. Schultz, A. W. Lichtenberger, J. W. Kooi, and C. K. Walker, "Beam lead fabrication for submillimeter-wave circuits using vacuum planarization," in *Proc. 14<sup>th</sup> Int. Symp. Space & THz Tech.*, Tucson, AZ, USA, 2003, pp. 499-501.
- [113] R. B. Bass, J. C. Schultz, A. W. Lichtenberger, R. M. Weikle, S.-K. Pan, E. Bryerton, C. K. Walker, and J. W. Kooi, "Ultra-thin silicon chips for submillimeter-wave applications," in *Proc. 15<sup>th</sup> Int. Symp. Space & THz Tech.*, Northampton, MA, USA, 2003, pp. 499-501.
- [114] J. Kooi, C. D. d'Aubigny, R. B. Bass, C. Walker, and A. W. Lichtenberger, "Large RF bandwidth waveguide to thinfilm microstrip transitions on suspended membrane for use in silicon micromachined mixer blocks at THz frequencies," in *Proc. 14<sup>th</sup> Int. Symp. Space THz Tech.*, Tucson, AZ, 2003.
- [115] P. H. Siegel, R. P. Smith, M. C. Gaidis, and S. C. Martin, "2.5-THz GaAs monolithic membrane-diode mixer," *IEEE Trans. Microwave Theory Tech.*, vol. 47, pp. 596-604, 1999.
- [116] G. Yassin and S. Withington, "Analytical expression for the input impedance of a microstrip probe in waveguide," *Int. J. Infrared Millimeter Waves*, vol. 17, pp. 1685-1705, 1996.
- [117] CST AG., *CST Studio Suite™ 2009*.

- [118] EMDS, "Agilent Technologies, Palo Alto, CA," 2000.
- [119] S. M. X. Claude and C. T. Cunningham, "Design of a Sideband-Separating Balanced SIS Mixer Based on Waveguide Hybrids," in *ALMA Memo 316*, 2000.
- [120] ANSYS Inc., *Southpointe, 275 Technology Drive, Canonsburg, PA 15317, USA*.
- [121] G. Oya and Y. Onodera, "Transition temperatures and crystal structures of single-crystal and polycrystalline NbN<sub>x</sub> films," *J. Appl. Phys.*, vol. 45, pp. 1389-1397, 1974.
- [122] P. Yagoubov, G. Gol'tsman, B. Voronov, L. Seidman, V. Siomash, S. Cherednichenko, and E. Gershenson, "The bandwidth of HEB mixers employing ultrathin NbN films on sapphire substrate," in *Proc. 7<sup>th</sup> Int. Symp. Space & THz Technol.*, 1996, pp. 290-302.
- [123] D. Bekermann, D. Barreca, A. Gasparotto, H. W. Becker, R. A. Fischer, and A. Devi, "Investigation of niobium nitride and oxy-nitride films grown by MOCVD," *Surface & Coatings Technol.*, vol. 204, pp. 404-409, 2009.
- [124] J. R. Gavalier, J. K. Hulm, M. A. Janocko, and C. K. Jones, "Preparation and superconducting properties of thin films of transition metal interstitial compounds," *J. Vac. Sci. Technol. B*, vol. 6, p. 177, 1969.
- [125] M. Juppo, M. Ritala, and M. Leskelä, "Use of 1,1-dimethylhydrazine in the atomic layer deposition of transition metal nitride thin films," *J. Electrochem. Soc.*, vol. 147, pp. 3377-3381, 2000.
- [126] R. E. Treece, J. S. Horwitz, J. H. Classen, and D. B. Chrsey, "Pulsed laser deposition of high-quality NbN thin films," *Appl. Phys. Lett.*, vol. 65, p. 2860, 1994.
- [127] J. R. Gao, M. Hajenius, F. D. Tichelaar, T. M. Klapwijk, B. Voronov, E. Grishin, G. Gol'tsman, C. A. Zorman, and M. Mehregany, "Monocrystalline NbN nanofilms on a 3C-SiC/Si substrate," *Appl. Phys. Lett.*, vol. 91, 2007.
- [128] A. Shoji, S. Kiryu, and S. Kohijiro, "Epitaxial growth of NbN and NbC<sub>x</sub>N<sub>1-x</sub> films on 3C-SiC film-covered Si wafers," *IEEE Trans Applied Superconductivity*, vol. 5, pp. 2396-2399, 1995.
- [129] J. R. Gao, M. Hajenius, F. D. Tichelaar, B. Voronov, E. Grishina, T. M. Klapwijk, G. Gol'tsman, and C. A. Zorman, "Can NbN films on 3C-SiC/Si change the IF bandwidth of hot electron bolometer mixers?," in *Proc. 17<sup>th</sup> Int. Symp. Space THz Technol.*, pp. 187-189, 2006.
- [130] Ultrasil Corporation, *3527 Breakwater Ave., Hayward, CA 94545, USA*.
- [131] F. Laermer and A. Schilp, "U.S. Patent No. (3, 26, ), "Method of anisotropically etching silicon." vol. 5501893 1996.
- [132] Norland Products, *2540 Route 139, Suite 100, Cranbury, NJ 08512, USA*.
- [133] MicroChem Corp., *1254 Chestnut Street Newton, MA 02464, USA*.